

Fluid deformation in isotropic Darcy flow

Daniel R. Lester^{1,†}, Marco Dentz², Aditya Bandopadhyay³ and Tanguy Le Borgne⁴

¹School of Engineering, RMIT University, 3000 Melbourne, Victoria, Australia

²Spanish National Research Council (IDAEA-CSIC), 08034 Barcelona, Spain

³Indian Institute of Technology Kharagpur (IITK), 721302 Kharagpur, India

⁴Geosciences Rennes, UMR 6118, Université de Rennes 1, CNRS, 35042 Rennes, France

(Received 26 June 2021; revised 21 June 2022; accepted 22 June 2022)

The deformation of fluid elements governs many processes in porous media, including the transport, dispersion and mixing of solutes, chemical reactions and colloidal particles. Recently, it has been shown that even in strongly heterogeneous porous media, steady three-dimensional (3-D) Darcy flow with isotropic hydraulic conductivity admits only constrained kinematics. This is due to its inherently helicity-free nature, as the velocity is everywhere orthogonal to the vorticity. This property precludes braided streamlines and instead admits a pair of coherent 3-D streamfunctions, and the streamlines cannot wander freely throughout the flow domain. In this study, we consider the impact of these kinematic constraints upon fluid deformation at the Darcy scale. We show that the helicity-free condition corresponds to an orthogonal 3-D streamline coordinate system, which we use to derive an *ab initio* continuous time random walk framework for fluid deformation. We find that the helicity-free condition combined with the intermittent nature of shear events leads to fluid deformation that is limited to algebraic growth, with stretching ranging from sublinear to superlinear behaviour. Fluid deformation in 3-D isotropic Darcy flow is remarkably similar to that of two-dimensional (2-D) Darcy flow, and the structure of 3-D Darcy flow is fundamentally the same as two superposed 2-D Darcy flows. These results have implications for understanding flow and transport in heterogeneous porous media, and provide a basis for quantification of mixing and dispersion in isotropic 3-D Darcy flow.

Key words: mixing and dispersion, porous media

† Email address for correspondence: daniel.lester@rmit.edu.au

© The Author(s), 2022. Published by Cambridge University Press. This is an Open Access article, distributed under the terms of the Creative Commons Attribution licence (<http://creativecommons.org/licenses/by/4.0/>), which permits unrestricted re-use, distribution and reproduction, provided the original article is properly cited.

1. Introduction

Mixing, dispersion and transport of diffusive solutes, colloids and heat in heterogeneous porous media are central to a myriad of processes in the natural environment and engineered applications (Bear 1972; Dagan 1989). These processes include chemical and biological reactions in geological substrates, pollution transport and remediation in groundwater flows, drug delivery in biological tissues, and electron transport in fuel cell applications (Cushman 2013). These processes all involve the interplay of molecular diffusion and hydrodynamic advection, where advection acts to organise the arrangement of fluid elements in a structured and deterministic manner (even if the porous medium is highly heterogeneous), and Brownian motion, which manifests as diffusion, acts to randomise solute molecules and colloidal particles. In particular, the deformation of fluid elements due to hydrodynamic advection plays a critical role with respect to solute mixing and dispersion processes, and indeed the characteristic rates of fluid deformation serve as input parameters to models (Villermaux & Duplat 2003; Le Borgne, Dentz & Villermaux 2013, 2015; Dentz *et al.* 2016*b*; Lester, Dentz & Le Borgne 2016*b*; Lester *et al.* 2018) of mixing and dispersion.

These quantitative measures describe the Lagrangian kinematics of the flow (Ottino 1989), which define the evolution, deformation and distribution of fluid elements from the Eulerian flow properties; the link between the Lagrangian kinematics and the Eulerian description of the flow can be complex and often non-intuitive (Aref 1984; Ottino 1989). Quantification of these kinematics and subsequent coupling with molecular or thermal diffusion then provides a means to predict the mixing (Villermaux 2012), dispersion (Dentz *et al.* 2018) and reaction of solutes (Engdahl, Benson & Bolster 2014) and colloids.

Over the past five decades, the interplay of these advection and diffusion processes has been well studied in the context of steady two-dimensional (2-D) flows at the Darcy scale (Dentz *et al.* 2000, 2018; Attinger, Dentz & Kinzelbach 2004; Beaudoin, de Dreuzy & Erhel 2010; Bijeljic, Mostaghimi & Blunt 2011; Cirpka *et al.* 2011; Chiogna *et al.* 2012; Villermaux 2012; De Anna *et al.* 2013; De Anna *et al.* 2014; Le Borgne *et al.* 2013), leading to important insights linking the nature, rate and extent of mixing, dispersion and transport to the underlying flow properties and ultimately, properties of the porous medium. However, such steady 2-D flows exhibit strongly constrained flow kinematics as streamlines are confined to the 2-D flow domain and cannot cross or diverge in an unbounded manner.

Conversely, while there are many studies of mixing, dispersion and transport in steady three-dimensional (3-D) flows (Gelhar & Axness 1983; Janković, Fiori & Dagan 2003; Englert, Vanderborcht & Vereecken 2006; Janković *et al.* 2009; Beaudoin & de Dreuzy 2013; Chiogna *et al.* 2014; Ye *et al.* 2015), the impact of possible kinematic constraints has received much less attention than its 2-D counterpart, and there is ongoing debate as to the nature of some transport processes (such as transverse macro-dispersion; Lowe & Frenkel 1996; Janković *et al.* 2009) in these flows. In general, extension to steady 3-D flows relaxes the kinematic constraints associated with steady 2-D flow, so streamlines may wander freely throughout the flow domain, and so can undergo braiding motions associated with chaotic advection (where exponential stretching of fluid elements rapidly accelerates diffusive mixing), diverge without bound (rapidly enhancing transverse dispersion), and generally exhibit a much richer array of Lagrangian kinematics (Aref *et al.* 2017). Hence solute mixing, dispersion and transport can be augmented significantly in steady 3-D flows in general.

Despite this potential for significantly augmented Lagrangian kinematics and solute mixing and transport dynamics, it has recently been shown (Lester *et al.* 2021) that steady 3-D Darcy flow in heterogeneous porous media with an isotropic hydraulic conductivity field admits highly constrained Lagrangian kinematics, similar to that of steady 2-D flow. These constraints arise as these flows all have vorticity that is everywhere orthogonal to their velocity, leading to zero helicity (an invariant measure of the topological complexity of a flow) across the entire class of isotropic Darcy flows. Lester *et al.* (2021) show that these helicity-free flows admit a pair of coherent streamfunctions that are topologically planar (although they may be highly convoluted in highly heterogeneous porous media), and the streamlines formed by intersections of the level sets (2-D streamsurfaces) of these streamfunctions are open and topologically equivalent to straight lines. Thus the confinement of streamlines to coherent 2-D streamsurfaces imposes kinematic constraints to steady 3-D isotropic Darcy flow that are very similar to those of steady 2-D flows.

While the study of Lester *et al.* (2021) generates insights into the Lagrangian kinematics of steady 3-D isotropic Darcy flow, an outstanding question is the quantitative impact of these kinematic constraints upon fluid deformation, which in turn govern mixing, dispersion and transport of diffusive solutes. In this study, we address this question by developing an orthogonal streamfunction coordinate system that inherently enforces the kinematic constraints of these flows. This coordinate system is then used to derive an *ab initio* coupled continuous time random walk (CTRW) model for fluid deformation that is in essence a 3-D extension of the fluid stretching model derived by Dentz *et al.* (2016b) for 2-D Darcy flow. When compared to general steady 3-D flows, we find that the kinematic constraints associated with steady 3-D isotropic Darcy flow severely retard fluid deformation, and so invite questions as to the suitability of isotropic Darcy flow as a representative model of flow and transport in highly heterogeneous porous media. These quantitative predictions of fluid deformation will be used in future studies to develop predictions of solute mixing and dispersion in isotropic 3-D Darcy flow.

We limit scope to steady 3-D isotropic Darcy flows with smooth and finite hydraulic conductivity fields in the absence of flow sources and sinks (and thus stagnation points) and domain boundaries, as many of these features can violate the helicity-free condition. Although this scenario does not arise commonly in practical applications, it does serve as an important case for understanding these fundamental issues. An important extension to this study is the analysis of the Lagrangian kinematics, mixing and dispersion at the Darcy scale in anisotropic porous media. These flows are not helicity free, and so are not subject to the same kinematic constraints as isotropic Darcy flow and are a subject of ongoing research. While many synthetic porous materials exhibit locally isotropic hydraulic conductivity, the majority of naturally occurring materials such as sedimentary rocks and natural fibres exhibit strongly anisotropic hydraulic conductivity (Bear 1972). Despite this, locally isotropic models are often employed in fundamental studies of solute transport and dispersion, and in applied studies when full characterisation of the hydraulic conductivity has not been performed. Hence it is important to understand the implications of using a locally isotropic model of hydraulic conductivity upon solute transport and mixing.

The remainder of this paper is structured as follows. In § 2, we review briefly the kinematics of isotropic Darcy flow from the study of Lester *et al.* (2021), and in § 3, we use these results to develop a streamfunction coordinate system that automatically imposes the kinematic constraints associated with isotropic Darcy flow. In this section, we address the long-standing question of whether helicity-free flows always give rise to a unique pair of

mutually orthogonal streamfunctions, and provide a geometric argument in the affirmative. In § 4, we then use these orthogonal streamfunctions as a basis for a coordinate system to generate closed-form solutions for the components of the fluid deformation gradient tensor. In § 5, we provide a numerical example to illustrate the deformation structure and orthogonality of the streamfunction coordinates for a model isotropic 3-D Darcy flow. An *ab initio* CTRW framework for the evolution of the deformation tensor in statistically stationary random flows is developed in § 6, and measures of transverse and longitudinal fluid deformation are introduced. Finally, conclusions are made in § 7.

2. The kinematics of 3-D isotropic Darcy flow

2.1. Governing equations and kinematics

To uncover the impact of kinematic constraints imposed by steady 3-D Darcy flow upon diffusive transport and mixing, in this section we briefly review the results of Lester *et al.* (2021) that the helicity- and stagnation-free nature of these flows admits a dual streamfunction representation. Steady 3-D Darcy flow in a heterogeneous porous medium with a scalar hydraulic conductivity field (henceforth described as isotropic Darcy flow) is described by the Darcy equation

$$\mathbf{v}(\mathbf{x}) = -(k(\mathbf{x})/\theta) \nabla \phi(\mathbf{x}), \quad (2.1)$$

where $\mathbf{x} = (x_1, x_2, x_3)$ denotes physical space in Cartesian coordinates, $\mathbf{v}(\mathbf{x})$ is the fluid velocity, $k(\mathbf{x})$ is the scalar hydraulic conductivity (which is positive and finite), θ is the porosity (henceforth assumed to be constant), and $\phi(\mathbf{x})$ is the pressure (or flow potential). As the velocity field \mathbf{v} is divergence-free, from (2.1) the flow potential ϕ satisfies the advection–diffusion equation

$$\nabla \cdot \mathbf{v} = \nabla^2 \phi + \nabla f \cdot \nabla \phi = 0, \quad (2.2)$$

where $f \equiv \ln(k/\theta)$. Two key properties of (2.1) significantly constrain the Lagrangian kinematics of isotropic Darcy flow. The first defining characteristic of Darcy flow is that it does not admit stagnation points in the flow (Bear 1972) in the absence of sources and sinks, and away from domain boundaries. This constrains the streamline topology, as recirculation regions cannot occur in the flow, so streamlines are open. The second defining characteristic of Darcy flow is that the helicity density $h(\mathbf{x})$ (defined as the dot product of velocity and vorticity) is everywhere zero (Moffatt 1969). This is shown by the vector identity

$$h \equiv \mathbf{v} \cdot \boldsymbol{\omega} = (k/\theta) \nabla \phi \cdot (\nabla \phi \times \nabla(k/\theta)) = 0, \quad (2.3)$$

where $\boldsymbol{\omega} \equiv \nabla \times \mathbf{v} = \nabla \phi \times \nabla k$ is the vorticity vector. The volume integral of the helicity density h over the flow domain Ω is defined as total helicity H (Moffatt 1969),

$$H = \int_{\Omega} h \, d\Omega, \quad (2.4)$$

which is an invariant measure of the topological complexity of the flow. Sposito (1994, 1997, 2001) recognised that the helicity-free nature of isotropic Darcy flow means that they have simple flow topology, and so proposed that these flows admit a lamellar set of non-intersecting Lamb surfaces (Lamb 1932) throughout the flow domain. These coherent material surfaces are spanned by streamlines and vorticity lines, and so organise streamlines of the flow and impose constraints on the Lagrangian kinematics.

These surfaces were then used in Lester *et al.* (2018) as a coordinate basis for a stochastic model of fluid deformation in isotropic 3-D Darcy flow. However, it was determined subsequently (Lester *et al.* 2019) that Lamb surfaces exist only for trivial isotropic 3-D Darcy flows, invalidating this stochastic model.

Subsequently, Lester *et al.* (2021) established that isotropic Darcy flows admit a pair of coherent 3-D streamfunctions. In this study, we use these streamfunctions as the basis for quantification of fluid deformation in isotropic Darcy flow, and so briefly review the basis for the existence of these streamfunctions as follows. Stagnation-free flows with zero helicity density are recognised to have integrable (Arnol'd 1965; Hénon 1966; Holm & Kimura 1991) particle trajectories, in the dynamical systems sense. This integrability condition (Arnol'd 1997) means that the 3-D advection equation

$$\frac{d\mathbf{x}}{dt} = \mathbf{v}[\mathbf{x}(t, t_0; \mathbf{X})], \quad \mathbf{x}(t_0, t_0; \mathbf{X}) = \mathbf{X}, \quad (2.5)$$

for the fluid tracer position $\mathbf{x}(t, t_0; \mathbf{X})$ (where \mathbf{X} gives the Lagrangian coordinates of the initial particle location) admits a pair of conserved quantities (invariants) denoted $\psi_1(\mathbf{x})$, $\psi_2(\mathbf{x})$ that may be interpreted as streamfunctions of the flow. Streamsurfaces then arise as level sets of these streamfunctions, and as the flow is stagnation free and helicity free (i.e. it does not possess knotted or closed flow paths), these streamsurfaces are topologically planar. Streamlines of the flow then arise at the intersection of ψ_1 and ψ_2 streamsurfaces, so these streamfunctions are constant along a streamline:

$$\psi_1(\mathbf{x}(t, t_0; \mathbf{X})) = \psi_1(\mathbf{X}), \quad \psi_2(\mathbf{x}(t, t_0; \mathbf{X})) = \psi_2(\mathbf{X}). \quad (2.6a,b)$$

The invariants (ψ_1 , ψ_2) allow the 3-D advection ordinary differential equation (2.5) to be simplified to the one-dimensional (1-D) definite integral (hence the terminology ‘integrable’)

$$\frac{ds}{dt} = v(s; \psi_1, \psi_2) \Rightarrow t(s) = \int_0^s \frac{1}{v(s; \psi_1, \psi_2)} ds, \quad (2.7)$$

where s is the distance travelled by a fluid particle along its trajectory, and $v(s; \psi_1, \psi_2)$ is the magnitude of the fluid velocity at distance s . The integrable nature of 3-D isotropic Darcy flow also means that chaotic advection is not possible in these flows as the braiding of streamlines is not possible, even if the hydraulic conductivity field is strongly heterogeneous.

This is in direct contrast to random pore-scale flows that have been shown (Lester, Trefry & Metcalfe 2016a; Lester *et al.* 2016b; Turuban *et al.* 2018, 2019; Heyman *et al.* 2020; Souzy *et al.* 2020; Heyman, Lester & Le Borgne 2021) to be inherently chaotic, even if the porous media is homogeneous at the pore scale. As stated by the Poincaré–Bendixson theorem, only continuous systems with three or more degrees of freedom can admit chaotic dynamics. Consequently, chaotic behaviour (even weakly so) is the norm rather than the exception in random systems with sufficient degrees of freedom. Conversely, the kinematic constraints associated with the helicity-free condition (2.3) in isotropic Darcy flow effectively reduce this three degrees of freedom system (associated with the three spatial dimensions) to a two degrees of freedom system that is not chaotic.

2.2. Streamfunction representation

An inherently divergence-free representation for the velocity field \mathbf{v} is given by the Euler representation

$$\mathbf{v} = -k \nabla \phi = \nabla \psi_1 \times \nabla \psi_2, \quad (2.8)$$

where the fluid velocity \mathbf{v} is orthogonal to the streamfunction gradients $\nabla \psi_1$ and $\nabla \psi_2$. The stagnation-free condition ($\mathbf{v} \neq \mathbf{0}$) for isotropic Darcy flow ensures that the streamfunctions is single-valued, i.e. $\nabla \psi_1 \neq \mathbf{0}$ and $\nabla \psi_2 \neq \mathbf{0}$. The helicity-free condition (2.3) has been used by several authors (Zijl 1986; Lester *et al.* 2021) to derive the following governing equations for the streamfunctions ψ_1 and ψ_2 :

$$\nabla^2 \psi_1 - \nabla f \cdot \nabla \psi_1 = \frac{(\mathbf{B} \times \nabla \psi_2) \cdot (\nabla \psi_1 \times \nabla \psi_2)}{\|\nabla \psi_1 \times \nabla \psi_2\|}, \quad (2.9)$$

$$\nabla^2 \psi_2 - \nabla f \cdot \nabla \psi_2 = \frac{(\mathbf{B} \times \nabla \psi_1) \cdot (\nabla \psi_1 \times \nabla \psi_2)}{\|\nabla \psi_1 \times \nabla \psi_2\|}, \quad (2.10)$$

where

$$\mathbf{B} \equiv (\nabla \psi_1 \cdot \nabla) \nabla \psi_2 - (\nabla \psi_2 \cdot \nabla) \nabla \psi_1. \quad (2.11)$$

Lester *et al.* (2021) showed that, to within numerical precision, solution of (2.9) and (2.10) yields the same velocity field \mathbf{v} as the solution of (2.2) for Darcy flow. In that study, it was shown that the integrable nature of isotropic Darcy flow implies that fluid deformation is limited to algebraic-in-time deformation, and that streamlines in porous media with statistically stationary hydraulic conductivity cannot converge or diverge without bound, leading to zero macroscopic transverse dispersion in the absence of diffusion. As such, the existence of the streamfunction pair (ψ_1, ψ_2) imposes significant constraints on the Lagrangian kinematics of isotropic Darcy flow. In this study, we quantify how these kinematics impact macroscopic mixing, dispersion and transport in the presence of local-scale dispersion. To quantify these impacts, in the next section we introduce a streamfunction coordinate system that automatically imposes the kinematic constraints inherent to heterogeneous isotropic Darcy flow.

3. Streamfunction coordinates

3.1. Uniqueness and orthogonality of streamfunction coordinates

In this section, we introduce a coordinate system for quantification of transport processes in 3-D isotropic Darcy flow. The existence of the streamfunction pair (ψ_1, ψ_2) generates a natural coordinate system that provides a convenient basis for the study of fluid deformation, mixing and dispersion in steady Darcy flows. Along with the flow potential ϕ , these streamfunctions form the curvilinear coordinate system (ϕ, ψ_1, ψ_2) that we term streamfunction coordinates. From (2.8), the streamfunction gradients are orthogonal to the potential gradient, but the streamfunction gradients are not mutually orthogonal as in general $\nabla \psi_1 \cdot \nabla \psi_2 \neq 0$. In Lester *et al.* (2021), it was shown that non-orthogonality between $\nabla \psi_1$ and $\nabla \psi_2$ significantly complicates the expression of spatial derivatives in the streamfunction coordinate system (ϕ, ψ_1, ψ_2) due to the presence off-diagonal terms in the metric tensor. However, the streamfunctions (ψ_1, ψ_2) are not unique, as demonstrated (Peymirat & Fontaine 1999) by the functions $\psi'_1(\psi_1, \psi_2)$ and $\psi'_2(\psi_1, \psi_2)$,

where

$$\nabla \psi'_1 \times \nabla \psi'_2 = \left(\frac{\partial \psi'_1}{\partial \psi_1} \frac{\partial \psi'_2}{\partial \psi_2} - \frac{\partial \psi'_2}{\partial \psi_1} \frac{\partial \psi'_1}{\partial \psi_2} \right) (\nabla \psi_1 \times \nabla \psi_2), \quad (3.1)$$

hence ψ'_1 and ψ'_2 are also streamfunctions if and only if

$$\frac{\partial \psi'_1}{\partial \psi_1} \frac{\partial \psi'_2}{\partial \psi_2} - \frac{\partial \psi'_2}{\partial \psi_1} \frac{\partial \psi'_1}{\partial \psi_2} = 1. \quad (3.2)$$

So there is an infinite set of streamfunctions that satisfy (2.8). The question of whether there exists a pair of mutually orthogonal streamfunctions (where $\nabla \psi'_1 \cdot \nabla \psi'_2 = 0$) amongst this set has been considered previously in the field of magnetic field topology, where the magnetic field vector \mathbf{B}_0 is represented in terms of the Euler potentials α and β as $\mathbf{B}_0 = \nabla \alpha \times \nabla \beta$. Rankin, Kabin & Marchand (2006) show that these potentials, along with the direction of the magnetic field, form an orthogonal coordinate system if and only if there exist no field-aligned magnetic currents. In the context of fluid mechanics, this corresponds to the zero helicity density condition (2.3). Similarly, Hui & Kudriakov (2001) and Hui & He (1997) argue that orthogonal streamline coordinates exist for helicity-free flows but do not provide an explicit proof *per se*.

Indeed, the general problem regarding the existence of a triply orthogonal system of surfaces (corresponding to the level sets of ϕ , ψ_1 and ψ_2) has a rich history dating back to the early nineteenth century, and has been addressed by many mathematicians, including Gauss, Lamé, Bonnet, Cayley and Darboux. Weatherburn (1926) shows that the so-called Lamé equations for the existence of triply orthogonal coordinates can be expressed in terms of a second-order differential equation for the unit normal \mathbf{n} projecting from one family of surfaces. In recent years, several studies have established a direct relationship between specific integrable systems and triply orthogonal coordinates (Terng & Uhlenbeck 1998), and there exist strong connections between classes of integrable systems and triply orthogonal coordinates (Zakharov 1998). Despite these advances, an explicit proof that helicity-free flows yield a triply orthogonal coordinate system is an outstanding problem.

In the following, we provide a geometric argument for the sufficient condition that helicity-free flows admit a pair of orthogonal streamfunctions, and in § 5, we show that this argument is satisfied for a numerically computed steady 3-D Darcy flow. In §§ 3.3 and 2 of the supplementary material (available at <https://doi.org/10.1017/jfm.2022.556>), we also prove the associated necessary condition that orthogonal streamline coordinates can yield only helicity-free flows. We begin by considering a 2-D isopotential surface \mathcal{S}_{ϕ^*} that corresponds to $\phi = \phi^* = \text{const.}$ Weatherburn (1926) shows that a family of non-intersecting surfaces exists in 3-D space if and only if the unit normal \mathbf{n} to one of the surfaces satisfies the condition of normality

$$\mathbf{n} \cdot (\nabla \times \mathbf{n}) = 0, \quad (3.3)$$

where the unit normal vector to \mathcal{S}_{ϕ^*} is given explicitly as $\mathbf{n} = \nabla \phi / |\nabla \phi| = \mathbf{v}/v$, and so (3.3) is satisfied directly by the helicity-free condition (2.3). Dupin's theorem states that 'orthogonal coordinate surfaces intersect along lines of principal curvature', so from the gauge freedom associated with the streamfunction coordinates (3.2), there exist two families of orthogonal curves (denoted respectively $(\psi_1^* = \text{const.}, \phi^*)$, $(\psi_2^* = \text{const.}, \phi^*)$) that may be identified as streamfunctions that foliate this isosurface via the lines of principal curvature and thus form a local 2-D orthogonal coordinate system on this surface. Thus, although two families of orthogonal curves can be easily constructed that foliate \mathcal{S}_{ϕ^*} ,

the question remains as to whether the curves (ψ_1^*, ϕ^*) , (ψ_2^*, ϕ^*) can be extended off \mathcal{S}_{ϕ^*} to form the pair of stream surfaces (ψ_1^*, ψ_2^*) that are both mutually orthogonal and normal to all other isopotential surfaces \mathcal{S}_{ϕ} .

This persistence of orthogonality of ψ_1^* , ψ_2^* corresponds to an angle-preserving transform between the curves (ψ_1^*, ϕ^*) , (ψ_2^*, ϕ^*) on \mathcal{S}_{ϕ^*} and the corresponding curves (ψ_1^*, ϕ^{**}) , (ψ_2^*, ϕ^{**}) on another arbitrary isopotential surface $\mathcal{S}_{\phi^{**}}$ (where $\phi^{**} = \text{const.}$). As the streamsurfaces ψ_1^* , ψ_2^* are invariant (material) surfaces, this angle-preserving (conformal) transform corresponds to irrotational flow (zero vorticity) within each isopotential surface \mathcal{S}_{ϕ} . Hence the helicity-free condition (2.3) may be interpreted as an angle-preserving transform from one isopotential surface to another (as the flow is irrotational in the plane normal to the flow direction, i.e. $\mathbf{v} \cdot \boldsymbol{\omega} = 0$). Hence if the streamfunctions ψ_1 , ψ_2 manifest as orthogonal curves on one isopotential surface, then ψ_1 , ψ_2 are mutually orthogonal for all isopotential surfaces. This angle-preserving property of helicity-free flows was also identified by Hui & Kudriakov (2001) and Hui & He (1997) in developing the argument that helicity-free flows admit orthogonal streamline coordinates.

In §§ 3.3 and 2 of the supplementary material, we develop the necessary proof that all orthogonal streamline coordinate systems of the form (ϕ, ψ_1, ψ_2) , where

$$\nabla\phi_1 \cdot \nabla\psi = 0, \quad \nabla\phi_2 \cdot \nabla\psi = 0, \quad \nabla\psi_1 \cdot \nabla\psi_2 = 0, \quad (3.4a-c)$$

render the helicity density to be zero. Whilst this necessary condition does not prove the sufficient condition that helicity-free flows guarantee the existence of an orthogonal streamfunction pair, we then assume the sufficient condition to hold based on the geometric argument above and those of Rankin *et al.* (2006), Hui & Kudriakov (2001) and Hui & He (1997). In § 5, we use a numerical example explicitly to show how a unique pair of orthogonal streamfunction coordinates arises in isotropic 3-D Darcy flow.

As the magnitude of the Darcy velocity $|\mathbf{v}|$ (and the pressure gradient $|\nabla\phi|$) must be positive and finite, from (2.8) the magnitude of the streamfunction gradients $|\nabla\psi_1|$, $|\nabla\psi_2|$ must also be everywhere positive and finite. In conjunction with the orthogonality condition (3.4a-c), this condition means that any point \mathbf{x}_0 in isotropic Darcy flow is defined uniquely by the local values of the fluid pressure and streamfunctions as $\boldsymbol{\xi}_0 \equiv (\phi(\mathbf{x}_0), \psi_1(\mathbf{x}_0), \psi_2(\mathbf{x}_0))$. Hence this set of scalar functions represents the orthogonal curvilinear streamfunction coordinate system

$$(\xi^1, \xi^2, \xi^3) \equiv (\phi, \psi_1, \psi_2), \quad \nabla\xi^i \cdot \nabla\xi^j = 0 \quad \text{for } i \neq j, \quad (3.5a,b)$$

which is invertible as the Jacobian $J \equiv \det[\mathbf{J}]$ (where $\mathbf{J} = \partial\xi^i/\partial x_j$ is the Jacobian matrix) is everywhere non-zero as $|\nabla\phi| \neq 0$, $|\nabla\psi_1| \neq 0$, $|\nabla\psi_2| \neq 0$ everywhere.

In § 3 of the supplementary material, we use the orthogonality condition (3.4a-c) to simplify the streamfunction governing equations (2.9) and (2.10) to the coupled equations

$$\nabla^2\psi_1 - \nabla(f - \ln|\nabla\psi_2|^2) \cdot \nabla\psi_1 = 0, \quad (3.6)$$

$$\nabla^2\psi_2 - \nabla(f - \ln|\nabla\psi_1|^2) \cdot \nabla\psi_2 = 0. \quad (3.7)$$

In § 4 of the supplementary material, it is shown that these governing equations enforce mutually orthogonal streamfunctions, $\nabla\psi_1 \cdot \nabla\psi_2 = 0$.

3.2. Scale factors and basis vectors

This coordinate system forms a convenient basis for studying the kinematics of isotropic Darcy flow as it naturally encodes the kinematic constraints of these flows, as will be

shown below. The mapping from Cartesian coordinates $\mathbf{x} \equiv (x_1, x_2, x_3)$ to streamfunction coordinates $\boldsymbol{\xi} \equiv (\xi^1, \xi^2, \xi^3)$ defines the metric tensor $g_{\alpha\beta}$, the elements of which determine the scale factors h_α of the transformation, such that the differential arc length ds in the coordinate system (ξ^1, ξ^2, ξ^3) is then given by $ds^2 = g_{\alpha\beta} d\xi^\alpha d\xi^\beta$. As the streamfunction and isopotential surfaces are orthogonal (3.4a–c), the covariant metric tensor is diagonal,

$$g_{\alpha\beta} = \begin{pmatrix} h_1^2 & 0 & 0 \\ 0 & h_2^2 & 0 \\ 0 & 0 & h_3^2 \end{pmatrix}, \tag{3.8}$$

and the components of the covariant $g_{\alpha\beta}$ and contravariant $g^{\alpha\beta}$ metric tensors are related as $g_{\alpha\alpha}^{-1} = g^{\alpha\alpha}$. The scale factors h_α of the streamfunction coordinate system are simply the spatial gradients of the fluid pressure ϕ and streamfunctions ψ_1, ψ_2 ,

$$h_\alpha = \sqrt{\sum_i \left(\frac{\partial x_i}{\partial \xi^\alpha}\right)^2} = \frac{1}{|\nabla \xi^\alpha|}, \quad \alpha = 1, 2, 3, \tag{3.9}$$

so

$$h_1 = \left| \frac{1}{\nabla \phi} \right| = \frac{ds}{d\phi}, \quad h_2 = \left| \frac{1}{\nabla \psi_1} \right| = \frac{dr}{d\psi_1}, \quad h_3 = \left| \frac{1}{\nabla \psi_2} \right| = \frac{dq}{d\psi_2}, \tag{3.10a–c}$$

where s, r, q , respectively, are the distances along a streamline, a vector line normal to a ψ_1 streamsurface, and that for a ψ_2 streamsurface. From (2.8), (3.10a–c) and the orthogonality condition (3.4a–c), these scale factors are related to the velocity and hydraulic conductivity k as $1/(h_2 h_3) = |\nabla \psi_1| |\nabla \psi_2| = v$, $h_1/(h_2 h_3) = |\nabla \psi_1| |\nabla \psi_2| / |\nabla \phi| = k$. Using (2.1) and (3.9), the scale factors h_α can be expressed without loss of generality as

$$h_1 = \frac{k}{v}, \quad h_2 = \sqrt{\frac{m}{v}}, \quad h_3 = \frac{1}{\sqrt{mv}}, \tag{3.11a–c}$$

where $m \equiv |\nabla \psi_2| / |\nabla \psi_1|$ is an arbitrary scalar function that quantifies the relative local spacing of the ψ_1 and ψ_2 streamsurfaces. In the streamfunction coordinate system, the covariant basis vectors \mathbf{g}_α are then

$$\mathbf{g}_\alpha = \left(\frac{\partial x_1}{\partial \xi^\alpha}, \frac{\partial x_2}{\partial \xi^\alpha}, \frac{\partial x_3}{\partial \xi^\alpha} \right), \quad \alpha = 1, 2, 3, \tag{3.12}$$

which are related to the unit covariant basis vectors $\hat{\mathbf{g}}_i$ and contravariant vectors \mathbf{g}^i via the scale factors h_α as

$$\hat{\mathbf{g}}_\alpha = \frac{1}{h_\alpha} \mathbf{g}_\alpha = h_\alpha \mathbf{g}^\alpha. \tag{3.13}$$

An arbitrary vector \mathbf{a} may be represented in terms of these basis vectors as $\mathbf{a} = a^i \mathbf{g}_i = a^{(i)} \hat{\mathbf{g}}_i = a_i \mathbf{g}^i$, with $a^{(i)} = h_i a^i = a_i / h_i$. The Jacobian J of the transform between Cartesian and streamfunction coordinates is then related to the determinant of the covariant metric tensor as $J = \sqrt{\det g_{\alpha\beta}} = h_1 h_2 h_3 = k/v^2$, and so is spatially variable. In §1 of the supplementary material, we use the above results to derive the divergence, gradient and curl operators in the streamfunction coordinate system.

3.3. Orthogonality of streamfunction coordinates

This orthogonal coordinate system automatically recovers the helicity-free condition as the velocity field is given as

$$\mathbf{v} = \nabla\psi_1 \times \nabla\psi_2 = \frac{1}{h_2h_3} \hat{\mathbf{g}}_2 \otimes \hat{\mathbf{g}}_3 = v\hat{\mathbf{g}}_1, \quad (3.14)$$

where $v = |\mathbf{v}|$, and from § 1 of the supplementary material, the vorticity is then

$$\boldsymbol{\omega} = \nabla \times \mathbf{v} = \frac{1}{h_1h_2h_3} \left\{ \frac{\partial(vh_1)}{\partial\psi_2} h_2\hat{\mathbf{g}}_2 - \frac{\partial(vh_1)}{\partial\psi_1} h_3\hat{\mathbf{g}}_3 \right\}. \quad (3.15)$$

Hence the helicity $h = \boldsymbol{\omega} \cdot \mathbf{v}$ is zero as the basis vectors $\hat{\mathbf{g}}_i$ are mutually orthogonal. As such, only helicity-free flows admit a pair of streamfunctions that are mutually orthogonal, and hence an orthogonal streamfunction coordinate system.

4. Fluid deformation in isotropic Darcy flow

4.1. Fluid deformation in Cartesian coordinates

As fluid mixing and dispersion arise from the interplay of diffusion and fluid deformation, in this section we develop expressions for the deformation of fluid elements in isotropic Darcy flow. The streamfunction coordinate system developed in § 2 forms a convenient basis for investigation of deformation of fluid elements in isotropic Darcy flow as the kinematic constraints associated with these flows are imposed automatically by the coordinate system. For simplicity of exposition, we first consider the deformation of fluid elements in the Cartesian coordinate system \mathbf{x} before extending this to the streamfunction coordinates $\boldsymbol{\xi}$, which as will be shown, presents significant simplification for the computation of fluid deformation. Such deformation is quantified by the fluid deformation gradient tensor $\mathbf{F}(\mathbf{X}, t)$, which quantifies how the infinitesimal vector $d\mathbf{x}(t; \mathbf{X})$ in the Eulerian frame deforms from its reference state $d\mathbf{X}(t = 0; \mathbf{X}) = d\mathbf{X}$ in the Lagrangian frame as

$$d\mathbf{x} = \mathbf{F}(\mathbf{X}, t) \cdot d\mathbf{X}, \quad (4.1)$$

and equivalently,

$$F_{ij} \equiv \frac{\partial x_i(t; \mathbf{X})}{\partial X_j}, \quad \mathbf{F}(\mathbf{X}, t) = \frac{\partial x_i(t; \mathbf{X})}{\partial X_j} \mathbf{e}_i \otimes \mathbf{e}^j, \quad (4.2a,b)$$

where $\hat{\mathbf{e}}_i = \mathbf{e}_i = \mathbf{e}^i$ respectively are the i th unit, covariant and contravariant vectors (which are all equal) in the Cartesian coordinate system. If we consider $\Phi_t(\mathbf{X})$ as the flow (in the dynamical systems sense of Arnol'd 1997) that maps the initial position \mathbf{X} of a fluid particle at time $t = 0$ to its current position \mathbf{x} at time t , then this flow is given as a solution of the advection equation (2.5), such that $\mathbf{x}(t, 0, \mathbf{X}) = \Phi_t(\mathbf{X})$ and so $\mathbf{X} = \Phi_{t=0}(\mathbf{X})$. From this definition, the deformation gradient tensor may also be defined by the derivative of

the flow with respect to the Lagrangian coordinate as

$$F(X, t) = \frac{\partial \Phi_t^i(X)}{\partial X^j} e_i \otimes e^j. \tag{4.3}$$

Following this definition, the deformation gradient tensor $F(t)$ evolves with travel time t along a Lagrangian trajectory (streamline) as

$$\frac{dF(X, t)}{dt} = \epsilon(t) \cdot F(X, t), \quad F(X, 0) = \mathbf{1}, \tag{4.4}$$

where $\epsilon(t)$ is the transpose of the velocity gradient tensor:

$$\epsilon(t) \equiv \nabla v(x(t; X))^T = \epsilon_{ij}(t) e_i \otimes e^j. \tag{4.5}$$

4.2. Fluid deformation in streamfunction coordinates

Solution of the deformation gradient evolution equation (4.4) is simplified greatly in the streamfunction coordinates, where we denote the Eulerian frame via the streamfunction coordinates $\xi = \{\xi^1, \xi^2, \xi^3\}$, and the corresponding Lagrangian frame in the streamfunction coordinates, $\Xi = \{\Xi^1, \Xi^2, \Xi^3\}$ (where $\xi = \Xi$ at $t = 0$). The corresponding flow in streamfunction coordinates is then denoted as $\xi = \chi_t(\Xi)$ (where $\Xi = \chi_{t=0}(\Xi)$), so the various frames are related as

$$\begin{array}{ccc} & \Xi^i & \xrightarrow{\xi^i = \chi_t^i(\Xi^j)} & \xi^i \\ \Xi^i(X^j) & \uparrow & & \downarrow \\ & X^i & \xrightarrow{x^i = \Phi_t^i(X^j)} & x^i \end{array} \quad x^i(\xi^j), \tag{4.6}$$

where the top and bottom rows, respectively, represent the streamfunction and Cartesian frames, and the left and right columns, respectively, represent the reference and current frames. In the streamfunction coordinate frame, the streamfunction deformation tensor $F(\Xi, t)$ relates the differential reference vector $d\Xi$ to its current configuration $d\xi$ as

$$F(\Xi, t) = \frac{\partial \xi_i(t; \Xi)}{\partial \Xi_j} g_i \otimes G^j, \tag{4.7}$$

where G^j is the j th contravariant vector of the streamfunction coordinate system in the Lagrangian frame (i.e. at $t = 0$). This deformation tensor may also be expressed in terms of the corresponding flow $\xi = \chi_t(\Xi)$ in streamfunction coordinates as

$$F(\Xi, t) = \frac{\partial \chi_t^i(\Xi)}{\partial \Xi^j} g_i \otimes G^j. \tag{4.8}$$

To render the components of the streamfunction deformation tensor physically meaningful, we express it in terms of the physical components $\hat{F}_{ij}(\Xi, t)$ as

$$F(\Xi, t) = \frac{\partial \chi_t^i(\Xi)}{\partial \Xi^j} \frac{h_i}{H_j} \hat{g}_i \otimes \hat{G}^j \equiv \hat{F}_{ij}(\Xi, t) \hat{g}_i \otimes \hat{G}^j, \tag{4.9}$$

where \hat{g}_i, \hat{G}^j are the respective unit vectors in the current and reference frames, and the corresponding scale factors are h_i, H_j . Following Marsden & Hughes (1994), the

streamfunction deformation gradient tensor can be translated into the Cartesian frame as

$$\begin{aligned}
 F(\boldsymbol{\Xi}, t) &= \frac{\partial \chi_t^i(\boldsymbol{\Xi})}{\partial \Xi^j} \mathbf{g}_i \otimes \mathbf{G}^j = \frac{\partial x^m}{\partial \xi^i} \frac{\partial \chi_t^i(\boldsymbol{\Xi})}{\partial \Xi^j} \frac{\partial \Xi^j}{\partial X^n} \mathbf{e}_m \otimes \mathbf{e}^n \\
 &= J_{mi}^{-1}(t) \frac{\partial \chi_t^i(\boldsymbol{\Xi})}{\partial \Xi^j} J_{kn}(0) \mathbf{e}_m \otimes \mathbf{e}^n = \frac{\partial \Phi_t^i(X)}{\partial X^j} \mathbf{e}_m \otimes \mathbf{e}^n = F(X, t), \quad (4.10)
 \end{aligned}$$

where $J_{ij}(t)$ is the ij th element of the Jacobian matrix at position $\mathbf{x}(t; X)$. Hence, as expected, the deformation gradient tensor is frame-indifferent. However, the elements of the physical deformation tensor transform between the Cartesian and streamfunction frames as

$$F_{mn}(X, t) = h_i J_{mi}^{-1}(t) \hat{F}_{ij}(\boldsymbol{\Xi}, t) H_J^{-1} J_{jn}(0) = \hat{J}_{mi}^{-1}(t) \hat{F}_{ij}(\boldsymbol{\Xi}, t) \hat{J}_{jn}(0), \quad (4.11)$$

where $\hat{J}_{ij}(t) = \nabla_i \xi_j / h_j$ represents the normalised Jacobian matrix that transforms physical vector components from the Cartesian to the streamfunction frame:

$$d\boldsymbol{\xi} = d\hat{\xi}_i \hat{\mathbf{g}}_i, \quad d\hat{\xi}_i = \hat{J}_{ij} x_j. \quad (4.12)$$

As $\det[\hat{J}_{ij}(t)] = 1$ and $\hat{J}_{ij}(t) \hat{J}_{ji}(t) = \delta_{ij}$, the normalised Jacobian represents a proper orthogonal transform that takes the form of a rotation matrix between the physical Cartesian and streamfunction frames. Correspondingly, differential vector elements in the four physical frames are then related as

$$\begin{array}{ccc}
 & d\hat{\Xi}^i & \xrightarrow{d\hat{\xi}^i = \hat{F}_{ij}(\boldsymbol{\Xi}, t) d\hat{\Xi}^j} & d\hat{\xi}^i \\
 d\Xi^i = \hat{J}_{ij}(0) dX^j & \uparrow & & \downarrow \\
 & dX^i & \xrightarrow{dx^i = F_{ij}(X, t) dX^j} & dx^i
 \end{array} \quad dx^i = \hat{J}_{ij}(t)^{-1} d\hat{\xi}^j. \quad (4.13)$$

Using (4.11), elements of the Cartesian deformation tensor can be determined by transforming the corresponding elements of the streamfunction deformation tensor via the Jacobian matrix in the reference and current frames. As indicated above, mapping of the differential element dX to dx is equivalent to first transforming dX to $d\boldsymbol{\Xi}$ via the Jacobian matrix at $t = 0$, then using the streamfunction deformation tensor to map to $d\boldsymbol{\Xi}$, and finally mapping back to dx via the inverse of the Jacobian matrix at $t = t$. Although this approach appears to be somewhat convoluted, the major advantage is that the Jacobian matrix is known everywhere and the deformation tensor F has an analytic solution in streamfunction coordinates, as will become clear in the following.

4.3. Solution of fluid deformation in streamfunction coordinates

Following (4.4), the physical components of the streamfunction deformation tensor evolve with time according to

$$\frac{dF(\boldsymbol{\Xi}, t)}{dt} = \boldsymbol{\epsilon}(t) \cdot F(\boldsymbol{\Xi}, t) \frac{d\hat{F}_{ij}(\boldsymbol{\Xi}, t)}{dt} = \hat{\epsilon}_{ij}(t) \hat{F}_{ij}(\boldsymbol{\Xi}, t), \quad \hat{F}_{ij}(\boldsymbol{\Xi}, 0) = \delta_{ij}, \quad (4.14a,b)$$

where $\boldsymbol{\epsilon}(t)$ is the velocity gradient tensor in streamfunction coordinates: $\boldsymbol{\epsilon}(t) = \epsilon_{ij}(t) \mathbf{g}_i \otimes \mathbf{g}^j = \hat{\epsilon}_{ij}(t) \hat{\mathbf{g}}_i \otimes \hat{\mathbf{g}}^j$, where $\hat{\epsilon}_{ij}(t) = h_i / h_j \epsilon_{ij}(t)$. From (1.12) in the supplementary material,

the gradient of a contravariant vector \mathbf{v} may be expressed in terms of the Christoffel symbols Γ_{jk}^i (Aris 1956; Nguyen-Schfer & Schmidt 2014) as

$$\nabla \mathbf{v} = \nabla(v^j \mathbf{g}_j) = \left(\frac{\partial v^i}{\partial \xi^j} + v^j \Gamma_{ij}^k \right) \mathbf{g}_i \otimes \mathbf{g}^j = \frac{h_i}{h_j} \left(\frac{\partial v^i}{\partial \xi^j} + v^j \Gamma_{ij}^k \right) \hat{\mathbf{g}}_i \otimes \hat{\mathbf{g}}^j, \quad (4.15)$$

and from (1.1) in the supplementary material, the fluid velocity \mathbf{v} in streamfunction coordinates simplifies to

$$\begin{aligned} \mathbf{v}(\phi, \psi_1, \psi_2) &= k \nabla \phi = \frac{k}{h_1} \hat{\mathbf{g}}_1 = v \hat{\mathbf{g}}_1, \\ &= \nabla \psi_1 \times \nabla \psi_2 = \frac{1}{h_2} \hat{\mathbf{g}}_2 \times \frac{1}{h_3} \hat{\mathbf{g}}_3 = \frac{1}{h_2 h_3} \hat{\mathbf{g}}_1 = v \hat{\mathbf{g}}_1. \end{aligned} \quad (4.16)$$

In § 5 of the supplementary material, (4.15) and (4.16) are used to derive the streamfunction velocity gradient tensor, which has non-zero physical components

$$\hat{\epsilon}_{11}(t) = \frac{\partial v}{\partial s}, \quad \hat{\epsilon}_{22}(t) = -\frac{1}{2} \frac{\partial v}{\partial s} + \frac{v}{2} \frac{\partial \ln m}{\partial s}, \quad \hat{\epsilon}_{33}(t) = -\frac{1}{2} \frac{\partial v}{\partial s} - \frac{v}{2} \frac{\partial \ln m}{\partial s}, \quad (4.17a-c)$$

$$\hat{\epsilon}_{12}(t) = 2\dot{\gamma}_r - \omega_r \equiv \sigma_r, \quad \hat{\epsilon}_{13}(t) = 2\dot{\gamma}_q - \omega_q \equiv \sigma_q, \quad (4.18a,b)$$

where $\dot{\gamma}$ and ω represent shear deformation and vorticity:

$$\dot{\gamma}_\alpha \equiv \frac{\partial v}{\partial \alpha}, \quad \omega_\alpha \equiv v \frac{\partial \ln k}{\partial \alpha}, \quad \alpha = r, q. \quad (4.19a,b)$$

In streamfunction coordinates, the velocity gradient $\epsilon(t)$ has a simple upper triangular structure

$$\epsilon(t) = \begin{pmatrix} \hat{\epsilon}_{11}(t) & \hat{\epsilon}_{12}(t) & \hat{\epsilon}_{13}(t) \\ 0 & \hat{\epsilon}_{22}(t) & 0 \\ 0 & 0 & \hat{\epsilon}_{33}(t) \end{pmatrix}, \quad (4.20)$$

where the diagonal components $\epsilon_{ii}(t)$ (with $\sum_i \epsilon_{ii} = 0$ due to incompressibility) correspond to normal fluid strains due to changes in velocity v and lateral expansion/contraction (as quantified by m) with distance s along a streamline. Conversely, the non-zero off-diagonal components σ_1, σ_2 are associated with shear $\dot{\gamma}_\alpha$ and vorticity ω_α (with $\alpha = r, q$) within the ψ_1 and ψ_2 streamsurfaces. Note that $\hat{\epsilon}_{23} = 0$ due to the helicity-free nature of the flow, hence there is no fluid shear in the direction orthogonal to the flow direction, and fluid deformation is decoupled between the (1, 2) and (1, 3) surfaces. As such, 3-D isotropic Darcy flow behaves as two superposed 2-D flows, and the kinematics of these flows is overwhelmingly 2-D in nature. We will show that this restriction has significant implications for fluid deformation, dispersion and mixing.

Several studies (Dentz *et al.* 2016b; Adachi 1986; Winter 1982) have shown that steady 2-D flows also admit an upper triangular velocity gradient tensor in streamline coordinates. Lester *et al.* (2018) also show that steady 3-D helicity-free flows have an upper triangular velocity gradient tensor in an orthogonal coordinate system comprised of velocity \mathbf{v} , vorticity $\boldsymbol{\omega}$ and the Lamb vector $\boldsymbol{\ell} \equiv \mathbf{v} \times \boldsymbol{\omega}$. However, it was shown subsequently (Lester *et al.* 2019) that the Lamb surfaces associated with the Lamb vector (where Lamb surfaces are level sets of the scalar potential field \mathcal{H} , and $\boldsymbol{\ell} = \nabla \mathcal{H}$) proposed by Sposito (1997, 2001) do not exist for general steady 3-D helicity-free flows, so the orthogonal vectors $(\mathbf{v}, \boldsymbol{\omega}, \boldsymbol{\ell})$ do not form a holonomic (coordinate) basis, and thus a coherent

coordinate system. Hence (4.20) is the first valid exposition that the velocity gradient tensor in 3-D isotropic Darcy flow (and indeed all helicity-free flows) is upper triangular and the coupling component $\hat{\epsilon}_{23}$ is zero.

The upper triangular structure of the velocity gradient tensor in (4.20) admits a particularly simple solution for the fluid deformation equation (4.4), in that the deformation gradient tensor is also upper triangular:

$$F(\boldsymbol{\Xi}, t) = \begin{pmatrix} \hat{F}_{11} & \hat{F}_{12} & \hat{F}_{13} \\ 0 & \hat{F}_{22} & 0 \\ 0 & 0 & \hat{F}_{33} \end{pmatrix}, \tag{4.21}$$

with $\det F(\boldsymbol{\Xi}, t) = \prod_i \hat{F}_{ii}(\boldsymbol{\Xi}, t) = 1$ due to incompressibility. The diagonal components of $F(\boldsymbol{\Xi}, t)$ are given by (4.4) as

$$\hat{F}_{ii}(\boldsymbol{\Xi}, t) = \exp \left[\int_0^t dt' \epsilon_{ii}(t') \right], \quad i = 1, 2, 3, \tag{4.22}$$

which can be solved explicitly via the change of variable $dt = ds/v$ to yield

$$\hat{F}_{11}(\boldsymbol{\Xi}, t) = \frac{v(t)}{v(0)}, \quad \hat{F}_{22}(\boldsymbol{\Xi}, t) = \sqrt{\frac{v(0)}{v(t)} \frac{m(t)}{m(0)}}, \quad \hat{F}_{33}(\boldsymbol{\Xi}, t) = \sqrt{\frac{v(0)}{v(t)} \frac{m(0)}{m(t)}}, \tag{4.23a-c}$$

where $v(t) = |\mathbf{v}(\boldsymbol{\xi}(t; \boldsymbol{\Xi}))|$ and $m(t) = m(\boldsymbol{\xi}(t; \boldsymbol{\Xi}))$. In statistically stationary and isotropic media, $v(t)$ and $m(t)$ fluctuate in a random and uncorrelated manner, hence the principal strains F_{ii} also fluctuate around a unit mean value due to local fluctuations in the fluid velocity field. As such, the ensemble average for the principal strains are all unity,

$$\langle \hat{F}_{ii}(\boldsymbol{\Xi}, t) \rangle = 1, \quad i = 1, 2, 3, \tag{4.24}$$

which is also reflected by the fact that all zero helicity density flows are non-chaotic (Arnol'd 1965), hence the infinite-time Lyapunov exponent is identically zero:

$$\lambda = \langle \ln \hat{F}_{22}(\boldsymbol{\Xi}, t) \rangle = -\langle \ln \hat{F}_{33}(\boldsymbol{\Xi}, t) \rangle = 0. \tag{4.25}$$

In contrast, the magnitude of the non-zero shear strains $\hat{F}_{12}, \hat{F}_{13}$ grow without bound as

$$\begin{aligned} \hat{F}_{12}(\boldsymbol{\Xi}, t) &= v(t) \int_0^t dt' \frac{\epsilon_{12}(t') \hat{F}_{22}(\boldsymbol{\Xi}, t')}{v(t')} = v(t) \sqrt{\frac{v(0)}{m(0)}} \int_0^t dt' \frac{\sigma_r(t') \sqrt{m(t')}}{v(t')^{3/2}}, \tag{4.26} \\ \hat{F}_{13}(\boldsymbol{\Xi}, t) &= v(t) \int_0^t dt' \frac{\epsilon_{13}(t') \hat{F}_{33}(\boldsymbol{\Xi}, t')}{v(t')} = v(t) \sqrt{v(0) m(0)} \int_0^t dt' \frac{\sigma_q(t')}{v(t')^{3/2} \sqrt{m(t')}}, \tag{4.27} \end{aligned}$$

where the shear rates are $\sigma_r(t) = \sigma_r(\boldsymbol{\xi}(t; \boldsymbol{\Xi}))$ and $\sigma_q(t) = \sigma_q(\boldsymbol{\xi}(t; \boldsymbol{\Xi}))$. As particle advection along a streamline is governed by the advection equation (2.5), these integrals may be reformulated according to $dt = ds/v(s)$, where s is the distance along a streamline,

leading to the spatial integrals

$$\hat{F}_{12}(s) = v(s) \sqrt{\frac{v(0)}{m(0)}} \int_0^s ds' \frac{\sigma_r(s') \sqrt{m(s')}}{v(s')^{5/2}}, \quad (4.28)$$

$$\hat{F}_{13}(s) = v(s) \sqrt{v(0)m(0)} \int_0^s ds' \frac{\sigma_q(s')}{v(s')^{5/2} \sqrt{m(s')}}. \quad (4.29)$$

Thus persistent fluid deformation in 3-D isotropic Darcy flows is due solely to the fluid shears $\sigma_r(s)$, $\sigma_q(s)$ that are oriented in the orthogonal (1, 2) and (1, 3) surfaces that are both parallel to the streamwise direction. An expression similar to (4.28) has been derived by Dentz *et al.* (2016b) for the deformation of material elements in 2-D steady heterogeneous flow in streamline coordinates. In the case of 2-D steady flow considered by Dentz *et al.* (2016b), the stretching factor $m(s)$ in (4.28) is omitted, and the denominator of the integral contains a factor v^3 rather than $v^{5/2}$. Note that fluid deformation in (1, 3) surfaces of 3-D isotropic Darcy flow (given by (4.29)) is very similar to that of (1, 2) deformation (given by (4.28)), with the only differences that $m(t) \mapsto 1/m(t)$ and $\sigma_r(t) \mapsto \sigma_q(t)$. Hence the extension from steady 2-D flow to steady isotropic 3-D Darcy flow involves additional shear deformation in the (1, 3)-plane (which is absent in 2-D), and a scaling factor $\sqrt{m(t)/m(0)}$ that reflects the fact that whilst the overall flow is volume-preserving, the (1, 2) and (1, 3) surfaces themselves are not necessarily area-preserving.

In random stationary 2-D flows, the shear rate $\sigma(s)$ has been shown (Dentz *et al.* 2016b) to fluctuate around a mean value of zero, whilst the inverse velocity magnitude $1/v$ (which corresponds to the waiting time distribution in a finite region of the flow) often follows a heavy-tailed distribution for heterogeneous porous media. Dentz *et al.* (2016b) show that for 2-D steady random flows, the correlation between fluid shear (σ) and velocity (as $1/v^3$) processes leads to persistent elongation of material elements despite the zero mean nature of the shear rate σ . For 2-D steady flows, the factors driving this $1/v^3 = (1/v)(1/v)(1/v)$ velocity dependence are as follows: (i) one factor $1/v$ arises from the increased residence time of fluid elements in low-velocity regions; (ii) a second factor $1/v$ arises from the compression of fluid elements in the streamwise direction while shear is being applied; and (iii) the third factor $1/v$ is associated with the divergence of streamlines in low-velocity regions. Hence episodes of low velocity (where the velocity can become vanishingly small) in 2-D steady random flows can lead to a significant amplification of shear deformation and persistent elongation of material elements in the streamwise direction.

The same basic mechanisms are at play in 3-D isotropic Darcy flow, with the exception that the third factor above has a different scaling, $1/v^{5/2} = (1/v)(1/v)(1/v^{1/2})$, where the third factor associated with streamline divergence in low-velocity regions has changed from $1/v$ to $1/v^{1/2}$ due to the introduction of the third spatial dimension. In the case of 3-D isotropic Darcy flow, there exist pairs of 2-D streamfunctions that diverge with changes in the local velocity (rather than divergence of 1-D streamlines in steady 2-D flow), as reflected by the scaling $|\nabla\psi_1||\nabla\psi_2| = v$ in (3.10a–c), so each set of streamsurfaces diverges with respect to v as $1/v^{1/2}$. Quantitative differences in the divergence of each set of streamsurfaces is quantified by the scalar function $m = |\nabla\psi_2|/|\nabla\psi_1|$ introduced in (3.10a–c). Thus, rather than $1/v$ for the third factor above for 2-D flows, the divergence of streamsurfaces leads to a factor $\sqrt{m/v}$, $1/(\sqrt{mv})$, respectively in the integrals of (4.28), (4.29). Similar to the 2-D case, for random stationary flows, the longitudinal shears σ_r ,

σ_q have zero mean (as the ensemble-averaged or spatially averaged flow is a translation flow with zero shear), and both the scale factor m and the fluid velocity v fluctuate in a stationary manner. However, the net result of the interactions above is that for 3-D isotropic Darcy flow, fluid stretching due to the shears σ_r, σ_q is amplified nonlinearly in low-velocity regions (by the term $v^{5/2}$ in (4.28), (4.29)), leading to persistent growth of material elements.

5. Fluid deformation and streamline structure: numerical example

These dynamics and the structure of isotropic Darcy flow are illustrated in figure 1, which depicts isotropic Darcy flow in a triply periodic unit cube (3-torus) $\mathbb{T}^3 : \mathbf{x} \equiv (x_1, x_2, x_3) = [0, 1] \times [0, 1] \times [0, 1]$, with the spatially periodic hydraulic log-conductivity field

$$\begin{aligned} f(\mathbf{x}) = & 2.3 \sin(2\pi(x_1 + 0.34)) \sin(4\pi(x_2 - 0.14)) \\ & + 0.9 \sin(2\pi(x_1 - 0.26)) \sin(2\pi(x_3 + 0.44)) \\ & - 1.5 \sin(4\pi(x_3 - 0.86)) \sin(2\pi(x_3 - 0.24)), \end{aligned} \quad (5.1)$$

shown in figure 1(a). Darcy flow in this porous medium is driven by the unit mean potential gradient $\tilde{\phi}(\mathbf{x}) = -x_1$, and the potential fluctuation $\tilde{\phi}(\mathbf{x})$ that results from spatial heterogeneity of the hydraulic log-conductivity field $f(\mathbf{x})$ (where $\phi(\mathbf{x}) = \tilde{\phi}(\mathbf{x}) + \tilde{\phi}(\mathbf{x})$) is given by the Darcy equation (2.2) as

$$\nabla^2 \tilde{\phi} + \nabla f \cdot \nabla \tilde{\phi} = \frac{\partial f}{\partial x_1}, \quad (5.2)$$

subject to periodic boundary conditions on \mathbb{T}^3 . Equation (5.2) is solved on a regular 256^3 finite difference grid (corresponding to a resolution of 64 grid points per correlation length of $f(\mathbf{x})$) via an iterative Krylov sparse method to precision 10^{-16} , and the corresponding potential field $\phi(\mathbf{x})$ is shown in figure 1(b). This grid resolution is required to generate a high-precision continuous potential field $\phi(\mathbf{x})$ via cubic interpolation from the grid values, and the velocity field is then given by (2.1). The corresponding relative divergence error $d(\mathbf{x}) \equiv \nabla \cdot \mathbf{v} / \|\nabla \mathbf{v}\|$ from a sample of 10^5 random points in the domain is found to have average error 0.05 %, and the helicity is identically zero.

Although this flow is solved numerically in terms of the flow potential ϕ rather than the orthogonal streamfunctions ψ_1, ψ_2 , the orthogonal structure of these streamfunctions can be visualised via the deformation structure of the flow. Equation (4.21) shows that in streamfunction coordinates, projection of the fluid deformation tensor $F(\mathbf{X}, t)$ onto an isopotential surface normal to the flow simply involves principal stretches in the ψ_1, ψ_2 directions,

$$F_{2-D}(\mathbf{X}, t) = \begin{pmatrix} \hat{F}_{22} & 0 \\ 0 & \hat{F}_{33} \end{pmatrix}, \quad (5.3)$$

as the helicity-free condition precludes transverse shear (as quantified by $\hat{F}_{23}, \hat{F}_{32}$). These principal stretches can be used to identify the unique orthogonal streamfunction coordinates in the computed Darcy flow. By computing the Cartesian deformation tensor $F(\mathbf{X}, t)$ along a Lagrangian trajectory (reference streamline) of the flow shown as the black line in figure 1(c), this deformation tensor can be rotated to align with the velocity vector, and the projection into the 2-D isosurface is taken (see § 6 of the supplementary material for details). The principal axes $\mathbf{d}_r(t), \mathbf{d}_q(t)$ associated with the resultant 2-D transverse

Fluid deformation in isotropic Darcy flow

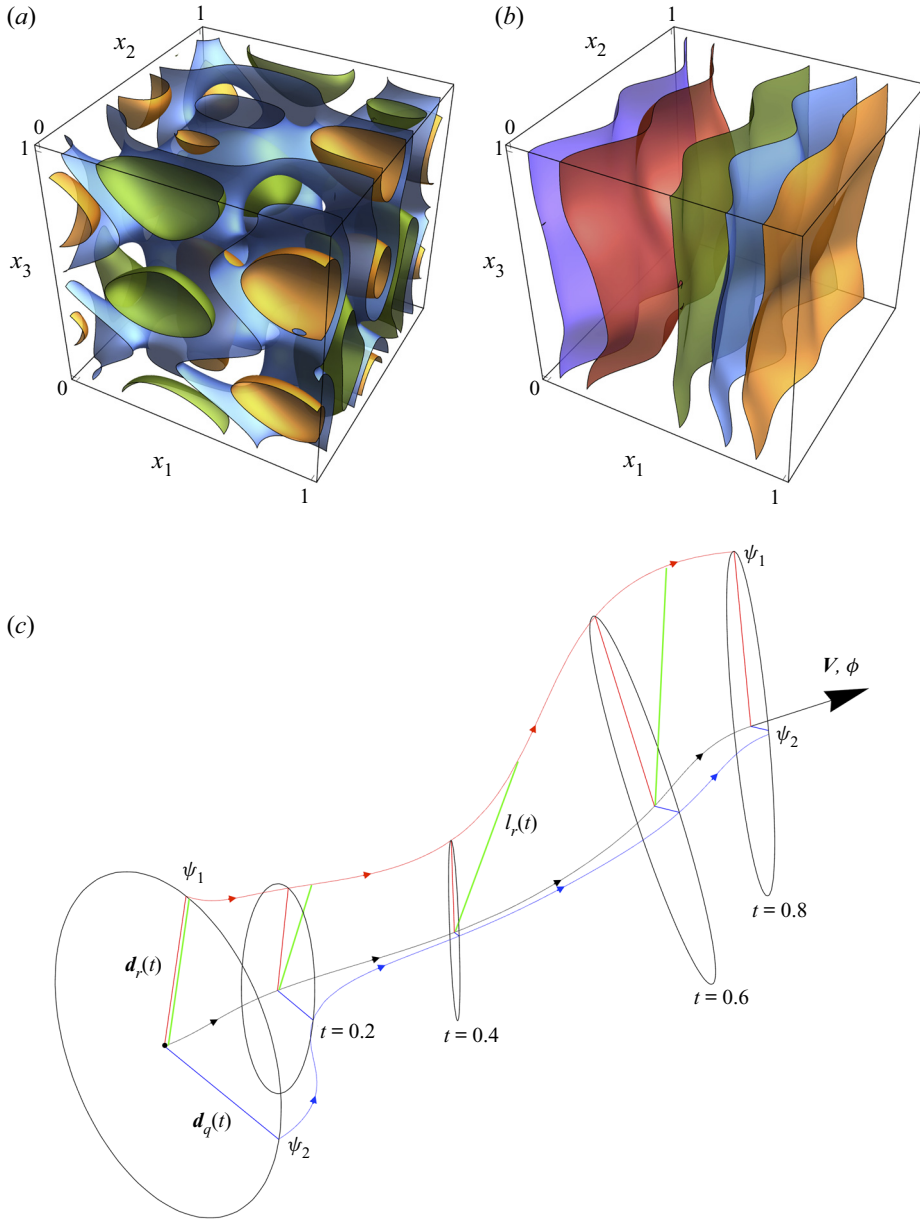


Figure 1. Isosurfaces of (a) the log-conductivity field $f(\mathbf{x})$ and (b) isopotential $\phi(\mathbf{x})$ surfaces for 3-D isotropic Darcy flow in a triply periodic unit cube. The streamline and deformation structure of this flow is shown in (c), where the reference streamline (black) is shadowed by two neighbouring streamlines that are offset in the ψ_1 (red) and ψ_2 (blue) directions. Note that the scale transverse to the black streamline has been amplified by a factor of 10^6 to aid visualisation, and the area of the ellipses scales inversely with fluid velocity \mathbf{v} . The black ellipses depict transverse fluid deformation at different time intervals from the reference state (circle) at the start (leftmost end) of the streamlines, and the principal axes of these ellipses (which define the ψ_1 and ψ_2 coordinate directions) are given by the deformation tensor components $\hat{F}_{22}(t)$, $\hat{F}_{33}(t)$. As shown, the red and blue streamlines always coincide with the principal axes of the deformation ellipses, thus maintaining orthogonality of the streamline coordinates throughout the flow domain. The green line in (c) depicts the evolution of a material line of length $l_r(t)$ that is initially oriented in the ψ_1 direction.

deformation tensor then identify the coordinate directions ψ_1, ψ_2 , and are related to the streamfunction deformation tensor components as

$$\hat{F}_{22}(t) = \frac{|\mathbf{d}_r(t)|}{|\mathbf{d}_r(0)|}, \quad \hat{F}_{33}(t) = \frac{|\mathbf{d}_q(t)|}{|\mathbf{d}_q(0)|}, \quad (5.4a,b)$$

As shown in figure 1(c), these principal axes $\mathbf{d}_r(t), \mathbf{d}_q(t)$ coincide with (red, blue) streamlines of the flow that are seeded at a distance of $\delta = 10^{-6}$ from the reference streamline (black) in the ψ_1, ψ_2 directions. As the principal axes $\mathbf{d}_r(t), \mathbf{d}_q(t)$ of the deformation ellipse are always orthogonal, orthogonality of the streamfunctions ψ_1, ψ_2 arises throughout the flow domain.

Figure 1 shows clearly the basis for the existence and persistence of mutually orthogonal streamfunctions in zero helicity flows. Here, the deformation transverse to the flow direction consists of only fluid stretching and/or contraction via the principal axes, so these principal axes form a continuous 2-D orthogonal coordinate system over an isopotential surface normal to the flow. The absence of rotation associated with vortical motion in these isopotential surfaces means that this 2-D orthogonal coordinate system then extends in the streamwise direction, thus forming a continuous 3-D orthogonal coordinate system that consists of the two families of streamsurfaces and the isopotential surfaces of the flow. However, unlike the case for non-orthogonal streamfunctions (Lester *et al.* 2021; Zijl 1986), presently there is no known set of partial differential equations to generate these orthogonal streamfunctions. The non-orthogonal streamfunctions (obtained by solution of (2.9), (2.10)) of a similar Darcy flow are shown in Figure 5(b) of (Lester *et al.* 2021), and the associated orthogonal streamfunctions are expected to have a similar structure. Fortunately, many of the theoretical results derived in this study in orthogonal streamfunction coordinates can be translated into the Cartesian frame and so can be used to understand and quantify the deformation structure of these flows.

Figures 2(a)–2(c) show the distribution of velocity magnitude $v(t)$, shear rates $\sigma_r(t), \sigma_q(t)$, and relative streamfunction gradients

$$\frac{|\nabla\psi_1(0)|}{|\nabla\psi_1(t)|} = \sqrt{\frac{v(0)m(t)}{v(t)m(0)}} = \frac{1}{\delta} |\mathbf{d}_r(t)|, \quad \frac{|\nabla\psi_2(0)|}{|\nabla\psi_2(t)|} = \sqrt{\frac{v(0)m(0)}{v(t)m(t)}} = \frac{1}{\delta} |\mathbf{d}_q(t)|, \quad (5.5a,b)$$

along the reference streamline shown in figure 1(c). Figure 2(d) shows the evolution of the lengths $l_r(t)$ and $l_q(t)$ of two material lines of initial length $\delta = 10^{-6}$ and respective orientation in the the ψ_1 and ψ_2 directions. As shown in figure 1(c), the lengths of these material lines evolve with changes in the streamline spacing (as quantified by $\hat{F}_{22}, \hat{F}_{33}$) and shear parallel to the streamwise direction (as quantified by $\hat{F}_{12}, \hat{F}_{13}$), and so are given explicitly as

$$l_r(t) = |\mathbf{F}(\mathbf{X}, t) \cdot \mathbf{d}_r(t)| = \delta\sqrt{\hat{F}_{12}(t)^2 + \hat{F}_{22}(t)^2}, \quad (5.6)$$

$$l_q(t) = |\mathbf{F}(\mathbf{X}, t) \cdot \mathbf{d}_q(t)| = \delta\sqrt{\hat{F}_{13}(t)^2 + \hat{F}_{33}(t)^2}, \quad (5.7)$$

where the initial persistent growth of $l_r(t)$ and $l_q(t)$ arises through $\hat{F}_{12}, \hat{F}_{13}$. Figure 2 shows clearly how fluid velocity, shear and streamline spacing control the growth of material lines as described by (4.26), (4.27). For example, the rapid growth of $l_r(t)$ and $l_q(t)$ over the time period $t \in [2, 3]$ corresponds to the low-velocity region in figure 2(a), and the

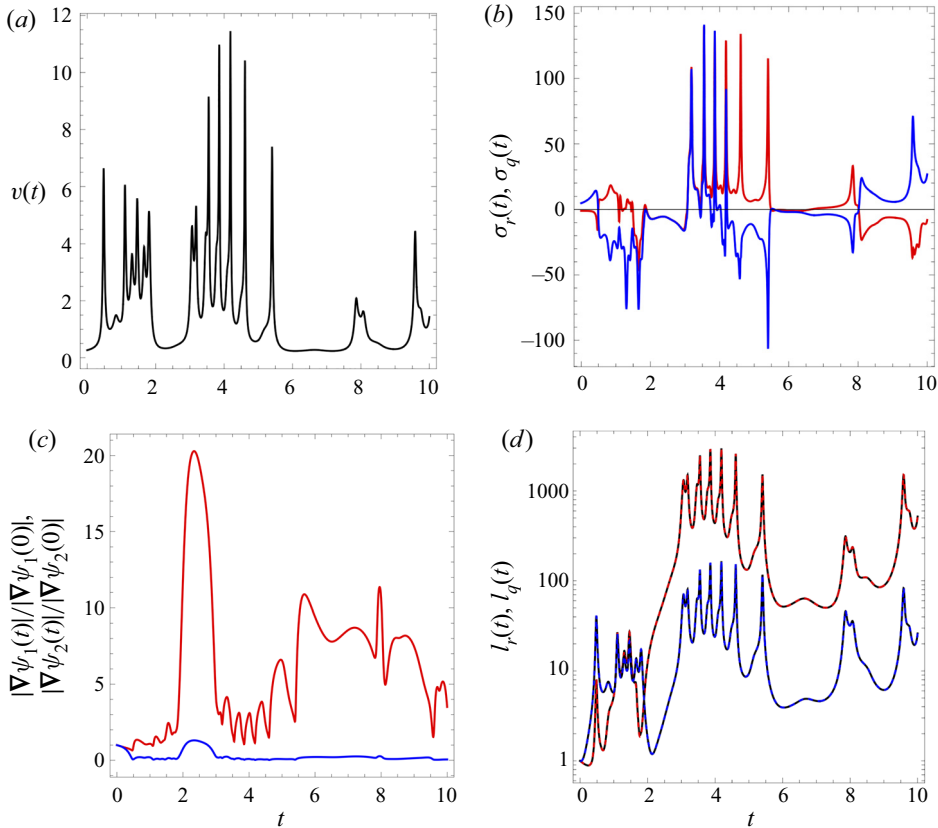


Figure 2. (a–c) Distributions along the black streamline shown in figure 1(c). (a) Distribution of velocity magnitude $v(t)$. (b) Distributions of shear rates: red line, $\sigma_r(t)$; blue line, $\sigma_q(t)$. (c) Distributions of streamfunction gradients: red line, $|\nabla\psi_1(t)|/|\nabla\psi_1(0)|$; blue line, $|\nabla\psi_2(t)|/|\nabla\psi_2(0)|$. (d) Evolution of the relative length $l(t)/l(0)$ of a differential line element oriented initially along the ψ_1 (red dashed line) and ψ_2 (blue dashed line) coordinates computed from (5.6), (5.7). These relative lengths very closely match those computed from both direct particle tracking (black lines) and the Cartesian deformation tensor (not shown, indistinguishable).

growth of $l_r(t)$ is more pronounced than that of $l_q(t)$ due to the larger streamfunction spacing in figure 2(c). Conversely, the low-velocity region in figure 2(a) over the period $t \in [6, 8]$ does not significantly alter $l_r(t)$ and $l_q(t)$ as the corresponding shear rates in figure 2(b) are both small. Figure 2(d) shows that the calculation of $l_r(t)$ and $l_q(t)$ agrees via: (i) computation of the Cartesian deformation tensor $F(X, t)$; (ii) computation of $\hat{F}_{12}(t)$, $\hat{F}_{13}(t)$, respectively, in (4.26), (4.27); and (iii) numerical calculation via particle tracking. Hence this agreement validates derivation of the evolution of the deformation gradient tensor in streamfunction coordinates in § 4. Note that although the flow field in this example is not random (due to the deterministic nature of the hydraulic conductivity field in (5.1)), the fluid velocity, shear rate and elongations along streamlines exhibit intermittent behaviour similar to that observed for steady random 3-D flows (Lester *et al.* 2018). For such random flows, intermittency of fluid velocity, shear rate and material deformation is due to the persistence of the flow velocity over the correlation scale of the hydraulic conductivity field and decorrelation over longer length scales. Such observations

form the basis for a stochastic model of fluid deformation in random isotropic 3-D Darcy flow that will be developed in the next section.

6. Fluid deformation as a continuous time random walk

For steady 3-D isotropic Darcy flow with a random stationary hydraulic conductivity field, the evolution of fluid velocity may be placed in a CTRW framework (Berkowitz *et al.* 2006). As fluid deformation is driven by the velocity gradient ∇v along streamlines, these processes may also be described by a CTRW process. In this section, we use the CTRW framework to develop closed-form predictions of fluid deformation in heterogeneous isotropic Darcy flow from the deformation evolution equations (4.28) and (4.29). At both the pore and Darcy scales, it is well established that the fluid velocity along a streamline in heterogeneous porous media follows a spatial Markov process (Le Borgne, Dentz & Carrera 2008a,b; De Anna *et al.* 2013; Edery *et al.* 2014; Kang *et al.* 2011; Hakoun, Comolli & Dentz 2019; Comolli, Hakoun & Dentz 2019). Coarse-graining particle motion on the order of the streamwise correlation length ℓ , the advection equation (2.5) may be described by the CTRW

$$s_{n+1} = s_n + \ell, \quad t_{n+1} = t_n + \frac{\ell}{v_n} \equiv t_n + \tau_n, \quad (6.1a,b)$$

where s_n is the spatial distance along a streamline at time t_n , v_n is the corresponding fluid velocity, and ℓ is the correlation length of the hydraulic conductivity field. Due to statistical stationarity of the conductivity field and Markovianity of the velocity distribution over distance ℓ , the velocities $v_n \equiv v(s_n)$ are identical independently distributed random variables distributed according to the probability density function (PDF) $p_v(v)$, which is related to the Eulerian velocity PDF $p_e(v)$ as $p_v(v) \propto v p_e(v)$ (Dentz *et al.* 2016a). For strongly heterogeneous media, the Eulerian velocity distribution shows algebraic behaviour for small velocities (Hakoun *et al.* 2019; Comolli *et al.* 2019). This implies that the PDF $\psi(t)$ of the temporal increment τ_n in (6.1a,b) is broadly distributed as

$$\psi(t) = \frac{\ell}{t^2} p_v\left(\frac{\ell}{t}\right). \quad (6.2)$$

6.1. Deformation evolution as a coupled continuous-time random walk

The coarse-grained equations of motion (6.1a,b) of a particle in the CTRW framework can also be used to coarse-grain the deformation evolution equations (4.28) and (4.29), resulting in

$$\hat{F}_{12}(s_n) \equiv \hat{F}_{12,n} = v_n \sqrt{v_0 m_0} I_{12,n}, \quad \hat{F}_{13}(s_n) \equiv \hat{F}_{13,n} = v_n \sqrt{\frac{v_0}{m_0}} I_{13,n}, \quad (6.3a,b)$$

where the coarse-grained integrals $I_{12,n}$ and $I_{13,n}$ in (4.28) and (4.29) are approximated as

$$I_{12,n} \approx \sum_{i=1}^n \rho_{r,n} \ell, \quad \rho_{r,n} \equiv \frac{\sigma_{r,n}}{\sigma_c} \left(\frac{v_c}{v_n}\right)^{5/2} \sqrt{\frac{m_n}{m_c}}, \quad (6.4a,b)$$

$$I_{13,n} \approx \sum_{i=1}^n \rho_{q,n} \ell, \quad \rho_{q,n} \equiv \frac{\sigma_{q,n}}{\sigma_c} \left(\frac{v_c}{v_n}\right)^{5/2} \sqrt{\frac{m_c}{m_n}}. \quad (6.5a,b)$$

Thus $I_{12,n}$ and $I_{13,n}$ satisfy the recursion relations

$$I_{12,n+1} = I_{12,n} + \rho_{r,n}\ell, \quad t_{n+1} = t_n + \frac{\ell}{v_n} = t_n + \tau_n, \quad (6.6a,b)$$

$$I_{13,n+1} = I_{13,n} + \rho_{q,n}\ell, \quad t_{n+1} = t_n + \frac{\ell}{v_n} = t_n + \tau_n, \quad (6.7a,b)$$

where the subscripts c and n on v , σ , m respectively denote characteristic values of these variables and their values at position s_n . Equations (6.6a,b) and (6.7a,b) are coupled CTRWs in the sense that the process increments $\rho_{r,n}$ and $\rho_{q,n}$ and the time increments τ_n are fully coupled via the local velocity v_n . Dentz *et al.* (2016b) assume that for steady 2-D flows, the absolute value of the shear rate σ_n is correlated strongly with the velocity magnitude v_n . For statistically isotropic Darcy flow, σ_r and σ_q have the same probability distribution. Indeed, for the model Darcy flow considered in § 5, σ_r and σ_q have the same distribution, and figure 3(a) indicates that both $|\sigma_r|$ and $|\sigma_q|$ are correlated strongly with the square of the velocity magnitude as $|\sigma_{r,n}|, |\sigma_{q,n}| \propto v_n^2$. In general, the shear rate may be correlated with the velocity magnitude as

$$|\sigma_{i,n}| = \zeta_n \sigma_c \left(\frac{v_n}{v_c} \right)^{\hat{\alpha}}, \quad i = (r, q), \quad (6.8)$$

where $\hat{\alpha} \approx 2, 1$ for 3-D and 2-D flows, respectively, and ζ_n is a random variable equal to ± 1 with equal probability. Equation (6.8) is a general power-law correlation between the local shear rate $\sigma_{i,n}$ and velocity v_n . Several studies (Dentz *et al.* 2016b; Lester *et al.* 2018) have found such a correlation to hold for steady random 2-D and 3-D flows. For statistically isotropic Darcy flows, the logarithm of the streamfunction relative gradient $\ln m_n$ is distributed symmetrically about $\ln m = 0$, so in conjunction with the equivalence of the distribution of $|\sigma_r|$ and $|\sigma_q|$, the increments ρ_r, ρ_q and thus the integrals I_{12}, I_{13} respectively have the same distributions. Indeed, figure 3(b) shows that for the model Darcy flow in § 5, the logarithm of the streamfunction relative gradient $\ln m_n$ follows a normal distribution with zero mean and variance $\sigma_{\ln m}^2 = 6.533$ and is found to be uncorrelated to velocity or shear rate. From (6.8), (6.4a,b) and (6.5a,b), the process increments $\rho_{i,n}$ in the coupled CTRWs (6.6a,b) and (6.7a,b) are related to the transition times $\tau_n = \ell/v_n$ as

$$\rho_{i,n} = \zeta_n \left(\frac{\tau_n}{\tau_v} \right)^\alpha, \quad \alpha = \frac{5}{2} - \hat{\alpha}, \quad i = (r, q), \quad (6.9)$$

where $\tau_v \equiv \ell/v_c$, $\langle \rho \rangle = 0$ and $|\rho_{i,n}| = (\tau_n/\tau_v)^\alpha$. In contrast to (6.9), for 2-D flows the index for the elongation increments is related to $\hat{\alpha}$ as $\alpha = 3 - \hat{\alpha}$ (Dentz *et al.* 2016b), reflecting the stronger coupling between low-velocity regions and fluid deformation in these flows. The joint PDF $\psi(\rho, \tau)$ of the process increments and transition times is then

$$\psi(\rho, \tau) = \frac{1}{2} \delta \left[|\rho| - \left(\frac{\tau}{\tau_v} \right)^\alpha \right] \psi(\tau). \quad (6.10)$$

Thus the index α can differ significantly between 2-D and 3-D flows: for 2-D flow, Dentz *et al.* (2016b) finds $\alpha = 3 - \hat{\alpha} = 2$, whereas for steady 3-D Darcy flow, $\alpha = 5/2 - \hat{\alpha}$. For the specific Darcy flow considered in § 5, it is observed in figure 3(a) that $\hat{\alpha} = 2$, hence $\alpha = 5/2 - \hat{\alpha} = 1/2$, but different values of α are possible for other steady isotropic 3-D Darcy flows. These differences in α can result in qualitative differences in the deformation

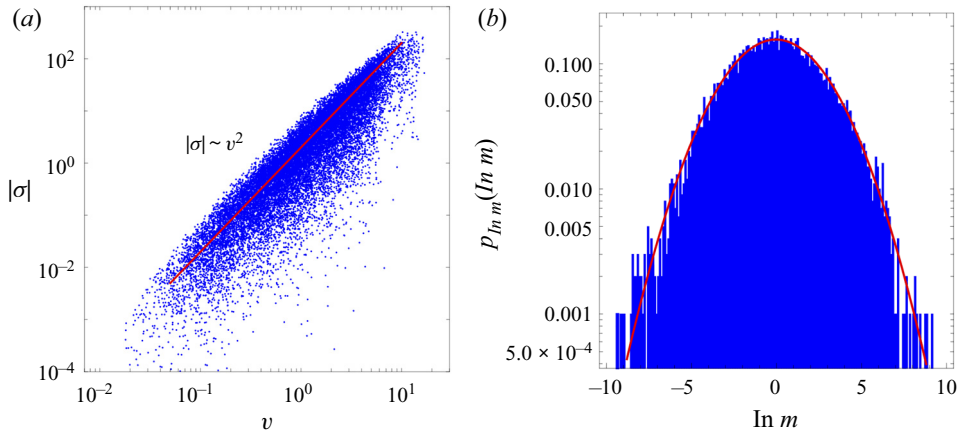


Figure 3. (a) Correlation between absolute shear rate $|\sigma(t)|$ and velocity $v(t)$, showing $\hat{\alpha} = 2$. (b) Distribution of relative streamfunction gradient $m(t) = |\nabla\psi_1|/|\nabla\psi_2|$ for the model 3-D Darcy flow considered in § 5.

behaviour in these flows. Many porous media flows, including heterogeneous Darcy flow (Hakoun *et al.* 2019), are characterised by a power-law velocity distribution $p_v(v) \propto (v/v_c)^{\beta-1}$ for velocities smaller than a characteristic velocity v_c , where β decreases with increasing heterogeneity of the hydraulic conductivity field. The corresponding transition time PDF scales as $\psi(\tau) \propto (\tau/\tau_v)^{-1-\beta}$ for $\tau > \tau_v$. Under these conditions, the CTRWs (6.6a,b) and (6.7a,b) describe a coupled Lévy walk (Dentz *et al.* 2015) for each of the deformation tensor components $\hat{F}_{12}, \hat{F}_{13}$ that is parametrised by α and β .

The dynamics of this class of coupled Lévy walk has been considered previously in detail by Dentz *et al.* (2015), so these results can be applied directly to the CTRWs (6.6a,b) and (6.7a,b). Dentz *et al.* (2015) derive a range of algebraic scaling behaviours for the moments of I_n that depend upon the parameters α and β , which have also been used by Dentz *et al.* (2016b) to quantify fluid deformation in steady 2-D flow. For the case of fluid deformation in steady isotropic 3-D Darcy flow, the results from Dentz *et al.* (2015) indicate that for $\alpha \geq 1$, the growth of the absolute value of the deformation components $\langle |\hat{F}_{1i}(t)| \rangle$ ranges from diffusive ($\langle |\hat{F}_{1i}(t)| \rangle \sim t^{1/2}$) to superlinear ($\langle |\hat{F}_{1i}(t)| \rangle \sim t^{1+\alpha-\beta}$) growth depending upon the relative magnitudes of α and β . For cases where $\alpha < 1$, Dentz *et al.* (2015) show that growth of the deformation components ranges from diffusive for $\beta > 2\alpha$ to dispersive for $1 < \beta < 2\alpha$ to weakly anomalous for $0 < \beta < 1$, where the deformation components evolve as $\langle |\hat{F}_{1i}(t)| \rangle \sim t^r$, with

$$r = \begin{cases} \alpha, & 0 < \beta < 1, \\ \frac{1}{2} + \alpha - \frac{\beta}{2}, & 1 < \beta < 2\alpha, \\ \frac{1}{2}, & 2\alpha < \beta. \end{cases} \quad (6.11)$$

These scalings are tested by comparison with numerical evaluation of the CTRWs (6.4a,b), (6.5a,b) for various values of α and β , and the results are shown in figure 4. As expected, (6.11) recovers the correct scaling behaviour of the absolute values of the integrals $|I_{12}|, |I_{13}|$ at long times, and the PDFs of $|I_{12}|, |I_{13}|$ at $t = 10^3$ are well described by a half-normal distribution. Thus fluid deformation in random stationary 3-D isotropic Darcy flows can admit a diverse range of behaviour ranging from diffusive to superlinear growth,

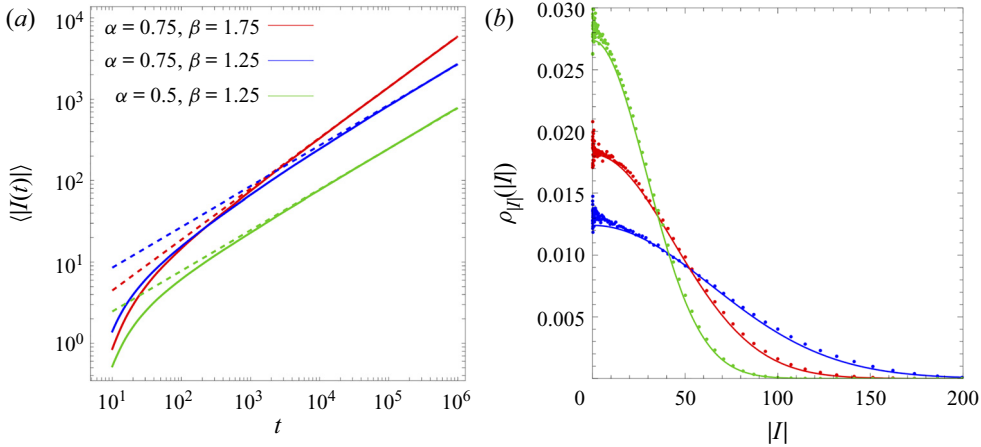


Figure 4. (a) Evolution of integrals $\langle |I(t)| \rangle = \langle |I_{12}(t)| \rangle = \langle |I_{13}(t)| \rangle$ from numerical solution of the CTRWs (6.6a,b), (6.7a,b) (solid lines) and comparison with scalings given by (6.11) (dashed lines) for various values of α and β . (b) PDF of $|I(t)|$ (points) and fitted half-normal distribution (lines) from numerical solution of (6.6a,b), (6.7a,b) for various values of α and β at $t = 10^3$.

depending upon the correlation between fluid shear and velocity (as characterised by α) and scaling of the velocity PDF in the small velocity regime (as characterised by β). This coupling leads to algebraic growth of the transverse deformation components as

$$\langle |\hat{F}_{12}(t)| \rangle \sim t^{r_2}, \quad \langle |\hat{F}_{13}(t)| \rangle \sim t^{r_3}, \quad (6.12a,b)$$

where the power-law indices $0 < r_2, r_3 < 2$ exhibit different scaling regimes (quantified by (Dentz *et al.* 2015)) that depend upon the specific values of α and β . It is useful to note that α appears to vary minimally from one medium to the next, whereas β decreases with increasing medium heterogeneity (Dentz *et al.* 2016b), hence it may be possible to approximate these parameters from field studies. Although there exist minor differences in values of these exponents for 2-D and 3-D isotropic Darcy flows, the basic mechanism of persistent deformation in 3-D Darcy flows is remarkably similar to that of 2-D flow, where intermittency of low-velocity regions can amplify fluid stretching nonlinearly due to shear oriented parallel to the streamwise direction. The power-law growth of $\hat{F}_{12}(t)$ and $\hat{F}_{13}(t)$ in (6.12a,b) is consistent with the theory (Arnol'd 1965; Ottino 1989) that all non-chaotic helicity-free steady flows involve fluid deformation that scales algebraically in time. The novelty of the CTRW framework is that it quantifies the scaling laws for fluid deformation, and facilitates identification of the mechanisms that govern the various scaling regimes.

6.2. Longitudinal and transverse deformation

To illustrate how the deformation tensor controls longitudinal and transverse deformation of fluid elements, we decompose $F(\mathbf{x}, t)$ into longitudinal and transverse components, respectively, as $F(\mathbf{x}, t) = F_l(\mathbf{x}, t) + F_t(\mathbf{x}, t)$, where

$$F_l(\mathbf{x}, t) \equiv \text{diag}(\hat{g}_1) \cdot F(\mathbf{x}, t) = \begin{pmatrix} \hat{F}_{11} & \hat{F}_{12} & \hat{F}_{13} \\ 0 & 0 & 0 \\ 0 & 0 & 0 \end{pmatrix}, \quad (6.13)$$

$$F_t(\boldsymbol{\mathcal{E}}, t) \equiv \text{diag}(\hat{\boldsymbol{g}}_2 + \hat{\boldsymbol{g}}_3) \cdot F(\boldsymbol{\mathcal{E}}, t) = \begin{pmatrix} 0 & 0 & 0 \\ 0 & \hat{F}_{22} & 0 \\ 0 & 0 & \hat{F}_{33} \end{pmatrix}, \quad (6.14)$$

where $\text{diag}(\boldsymbol{a})$ is a diagonal matrix comprised of the vector \boldsymbol{a} along the diagonal. From (4.1), a differential line element $\delta I(\boldsymbol{\mathcal{E}}, t)$ at Lagrangian position $\boldsymbol{\mathcal{E}}$ at time $t = 0$ evolves with time as

$$\begin{aligned} \delta I(\boldsymbol{\mathcal{E}}, t) &= F(\boldsymbol{\mathcal{E}}, t) \cdot \delta I(\boldsymbol{\mathcal{E}}, 0) = F_l(\boldsymbol{\mathcal{E}}, t) \cdot \delta I(\boldsymbol{\mathcal{E}}, 0) + F_t(\boldsymbol{\mathcal{E}}, t) \cdot \delta I(\boldsymbol{\mathcal{E}}, 0) \\ &\equiv \delta I_l(\boldsymbol{\mathcal{E}}, t) + \delta I_t(\boldsymbol{\mathcal{E}}, t), \end{aligned} \quad (6.15)$$

and so may be decomposed into its longitudinal $\delta I_l(\boldsymbol{\mathcal{E}}, t)$ and transverse $\delta I_t(\boldsymbol{\mathcal{E}}, t)$ components. Similarly, the length $\delta l(t)$ of these line elements can also be decomposed as $\delta l(t)^2 = \delta I_l(t)^2 + \delta I_t(t)^2$ via

$$\begin{aligned} \delta l(t) &\equiv |\delta I(\boldsymbol{\mathcal{E}}, t)| = \sqrt{\delta I(\boldsymbol{\mathcal{E}}, 0) \cdot (F_l^T(\boldsymbol{\mathcal{E}}, t) \cdot F_l(\boldsymbol{\mathcal{E}}, t) + F_t^T(\boldsymbol{\mathcal{E}}, t) \cdot F_t(\boldsymbol{\mathcal{E}}, t)) \cdot \delta I(\boldsymbol{\mathcal{E}}, 0)} \\ &\equiv \sqrt{\delta I_l(t)^2 + \delta I_t(t)^2}. \end{aligned} \quad (6.16)$$

From (6.15), we characterise longitudinal and transverse fluid deformation respectively in terms of the metrics $\Lambda_l(t)$, $\Lambda_t(t)$ as

$$\Lambda_l(t) \equiv \left\langle \frac{\delta I_l(t)}{\delta I_l(0)} \right\rangle = \langle \|F_l(\boldsymbol{\mathcal{E}}, t)\| \rangle = \langle \sqrt{\hat{F}_{11}(\boldsymbol{\mathcal{E}}, t)^2 + \hat{F}_{12}(\boldsymbol{\mathcal{E}}, t)^2 + \hat{F}_{13}(\boldsymbol{\mathcal{E}}, t)^2} \rangle, \quad (6.17)$$

$$\Lambda_t(t) \equiv \left\langle \frac{\delta I_t(t)}{\delta I_t(0)} \right\rangle = \langle \|F_t(\boldsymbol{\mathcal{E}}, t)\| \rangle = \langle \sqrt{\hat{F}_{22}(\boldsymbol{\mathcal{E}}, t)^2 + \hat{F}_{33}(\boldsymbol{\mathcal{E}}, t)^2} \rangle, \quad (6.18)$$

where $\Lambda_l(t)$ characterises the longitudinal stretching of fluid elements along streamlines due to shear and vorticity, whereas $\Lambda_t(t)$ characterises the transverse deformation due to the separation of streamlines. In Lester *et al.* (2018), we show that the growth rates of these differential deformation metrics are important for different applications. For the pulsed injection of a tracer, growth of the longitudinal metric $\Lambda_l(t)$ governs longitudinal mixing and dispersion of the resultant solute plume. For steady 2-D Darcy flow, the mean and variance of the growth of $\Lambda_l(t)$ act as inputs (along with the Péclet number Pe) for predictive models (Le Borgne *et al.* 2013, 2015) of mixing and dispersion in 2-D Darcy flow. Conversely, for continuous injection of a tracer, the growth rate of the transverse element $\Lambda_t(t)$ characterises the transverse mixing and dispersion of the plume. Along with the Péclet number Pe , the mean and variance of the growth rate of $\Lambda_t(t)$ are used by Lester *et al.* (2016b) to predict mixing of a continuously injected source in steady 3-D pore-scale flow. From (4.24) and (6.12a,b), we find that for 3-D steady isotropic Darcy flow, the longitudinal deformation of fluid elements can grow algebraically, whereas the transverse deformation of fluid elements is zero:

$$\Lambda_l(t) \sim t^r, \quad \Lambda_t(t) \sim 1. \quad (6.19a,b)$$

In conjunction with molecular diffusion, these deformation rates control the dispersion and mixing of solutes and colloids in isotropic Darcy flow.

7. Conclusions

We have considered the impacts of the Lagrangian kinematics of steady 3-D isotropic Darcy flow upon fluid deformation in isotropic heterogeneous porous media. These flows

are characterised by the fact that they are helicity free in that the velocity is everywhere orthogonal to the vorticity, which severely constrains their kinematics. These flows admit a pair of coherent streamfunctions. The intersection of their corresponding streamsurfaces forms highly constrained streamlines that cannot be knotted or braided. Furthermore, as pairs of streamlines cannot diverge, there is zero transverse macro-dispersion. This behaviour arises as streamlines of isotropic Darcy flow are confined to coherent 2-D streamsurfaces that are topologically planar, hence many of the kinematic constraints of 2-D steady flows apply to steady isotropic 3-D Darcy flow. To quantify the impact of these kinematic constraints upon fluid deformation, solute mixing and dispersion, we have used the properties of isotropic Darcy flows to develop an orthogonal coordinate system (comprised of the two streamfunctions and fluid pressure) that imposes automatically the kinematic constraints of these flows. We use this coordinate system to solve the fluid deformation evolution equations in 3-D isotropic Darcy flow, and find that it is remarkably similar to 2-D Darcy flow in that fluid elements do not persistently deform transversely (consistent with zero transverse macro-dispersion), and deform longitudinally only due to shear flow parallel to the flow direction. We develop a coupled continuous time random walk (CTRW) framework to describe the evolution of fluid deformation in the streamfunction coordinates, and show how the structure of these flows controls this process. We introduce measures of ensemble-averaged longitudinal ($\Lambda_l(t)$) and transverse ($\Lambda_t(t)$) fluid deformation, and show that although transverse deformation is zero ($\Lambda_t(t) \sim 1$), longitudinal deformation grows algebraically at a rate that can range from sub-diffusive to ballistic ($\Lambda_l(t) \sim t^r$, $r \in [0, 2]$), and the various scalings match direct numerical calculations of the stretching CTRW. Similar to steady 2-D flow (Dentz *et al.* 2016b), the stretching index r is controlled by intermittency of the fluid velocity and its correlation with the local shear field. These findings shed light onto the deformation dynamics of steady 3-D isotropic Darcy flows, and provide a basis for quantitative prediction of solute mixing, dispersion and transport in strongly heterogeneous porous media.

Supplementary material. Supplementary material is available at <https://doi.org/10.1017/jfm.2022.556>.

Funding. This work was supported by the European Research Council (T.L.B., grant no. 648377) and the Spanish Ministry of Science and Innovation (M.D., grant no. PID2019-106887GB-C31).

Declaration of interests. The authors report no conflict of interest.

Author ORCID*s*.

 Daniel R. Lester <https://orcid.org/0000-0003-2927-1384>;

 Marco Dentz <https://orcid.org/0000-0002-3940-282X>.

REFERENCES

- ADACHI, K. 1986 A note on the calculation of strain histories in orthogonal streamline coordinate systems. *Rheol. Acta* **25** (6), 555–563.
- AREF, H. 1984 Stirring by chaotic advection. *J. Fluid Mech.* **143**, 1–21.
- AREF, H., *et al.* 2017 Frontiers of chaotic advection. *Rev. Mod. Phys.* **89** (2), 025007.
- ARIS, R. 1956 On the dispersion of a solute in a fluid flowing through a tube. *Phil. Trans. R. Soc. A: Math. Phys. Engng Sci.* **235**, 67–77.
- ARNOL'D, V.I. 1965 Sur la topologie des écoulements stationnaires des fluides parfaits. *C. R. Acad. Sci. Paris* **261**, 312–314.
- ARNOL'D, V.I. 1997 *Mathematical Methods of Classical Mechanics*, 2nd edn, vol. 261. Springer.
- ATTINGER, S., DENTZ, M. & KINZELBACH, W. 2004 Exact transverse macro dispersion coefficients for transport in heterogeneous porous media. *Stoch. Environ. Res. Risk Assess.* **18** (1), 9–15.

- BEAR, J. 1972 *Dynamics of Fluids in Porous Media*. Dover Classics of Science and Mathematics, vol. 1. Dover.
- BEAUDOIN, A. & DE DREUZY, J.-R. 2013 Numerical assessment of 3-D macrodispersion in heterogeneous porous media. *Water Resour. Res.* **49** (5), 2489–2496.
- BEAUDOIN, A., DE DREUZY, J.-R. & ERHEL, J. 2010 Numerical Monte Carlo analysis of the influence of pore-scale dispersion on macrodispersion in 2-D heterogeneous porous media. *Water Resour. Res.* **46** (12), W12537.
- BERKOWITZ, B., CORTIS, A., DENTZ, M. & SCHER, H. 2006 Modeling non-Fickian transport in geological formations as a continuous time random walk. *Rev. Geophys.* **44** (2), RG2003.
- BIJELJIC, B., MOSTAGHIMI, P. & BLUNT, M.J. 2011 Signature of non-Fickian solute transport in complex heterogeneous porous media. *Phys. Rev. Lett.* **107**, 204502.
- CHIOGNA, G., HOCHSTETLER, D.L., BELLIN, A., KITANIDIS, P.K. & ROLLE, M. 2012 Mixing, entropy and reactive solute transport. *Geophys. Res. Lett.* **39**, L20405.
- CHIOGNA, G., ROLLE, M., BELLIN, A. & CIRPKA, O.A. 2014 Helicity and flow topology in three-dimensional anisotropic porous media. *Adv. Water Resour.* **73**, 134–143.
- CIRPKA, O.A., DE BARROS, F.P.J., CHIOGNA, G., ROLLE, M. & NOWAK, W. 2011 Stochastic flux-related analysis of transverse mixing in two-dimensional heterogeneous porous media. *Water Resour. Res.* **47** (6), W06515.
- COMOLLI, A., HAKOUN, V. & DENTZ, M. 2019 Mechanisms, upscaling, and prediction of anomalous dispersion in heterogeneous porous media. *Water Resour. Res.* **55** (10), 8197–8222.
- CUSHMAN, J.H. 2013 *The Physics of Fluids in Hierarchical Porous Media: Angstroms to Miles*, vol. 10. Springer Science & Business Media.
- DAGAN, G. 1989 *Flow and Transport in Porous Formations*. Springer.
- DE ANNA, P., JIMENEZ-MARTINEZ, J., TABUTEAU, H., TURUBAN, R., BORGNE, T.L., DERRIEN, M. & MEHEUST, Y. 2014 Mixing and reaction kinetics in porous media: an experimental pore scale quantification. *Environ. Sci. Technol.* **48** (1), 508–516.
- DE ANNA, P., LE BORGNE, T., DENTZ, M., TARTAKOVSKY, A.M., BOLSTER, D. & DAVY, P. 2013 Flow intermittency, dispersion, and correlated continuous time random walks in porous media. *Phys. Rev. Lett.* **110**, 184502.
- DENTZ, M., DE BARROS, F.P.J., LE BORGNE, T. & LESTER, D.R. 2018 Evolution of solute blobs in heterogeneous porous media. *J. Fluid Mech.* **853**, 621–646.
- DENTZ, M., KANG, P.K., COMOLLI, A., LE BORGNE, T. & LESTER, D.R. 2016a Continuous time random walks for the evolution of Lagrangian velocities. *Phys. Rev. Fluids* **1**, 074004.
- DENTZ, M., KINZELBACH, H., ATTINGER, S. & KINZELBACH, W. 2000 Temporal behavior of a solute cloud in a heterogeneous porous medium: 1. Point-like injection. *Water Resour. Res.* **36** (12), 3591–3604.
- DENTZ, M., LE BORGNE, T., LESTER, D.R. & DE BARROS, F.P.J. 2015 Scaling forms of particle densities for Lévy walks and strong anomalous diffusion. *Phys. Rev. E* **92**, 032128.
- DENTZ, M., LESTER, D.R., LE BORGNE, T. & DE BARROS, F.P.J. 2016b Coupled continuous-time random walks for fluid stretching in two-dimensional heterogeneous media. *Phys. Rev. E* **94**, 061102.
- EDERY, Y., GUADAGNINI, A., SCHER, H. & BERKOWITZ, B. 2014 Origins of anomalous transport in heterogeneous media: structural and dynamic controls. *Water Resour. Res.* **50** (2), 1490–1505.
- ENGDAHL, N.B., BENSON, D.A. & BOLSTER, D. 2014 Predicting the enhancement of mixing-driven reactions in nonuniform flows using measures of flow topology. *Phys. Rev. E* **90**, 051001.
- ENGLERT, A., VANDERBORGHT, J. & VERECKEN, H. 2006 Prediction of velocity statistics in three-dimensional multi-Gaussian hydraulic conductivity fields. *Water Resour. Res.* **42** (3), W03418.
- GELHAR, L.W. & AXNESS, C.L. 1983 Three-dimensional stochastic analysis of macrodispersion in aquifers. *Water Resour. Res.* **19** (1), 161–180.
- HAKOUN, V., COMOLLI, A. & DENTZ, M. 2019 Upscaling and prediction of Lagrangian velocity dynamics in heterogeneous porous media. *Water Resour. Res.* **55**, 3976–3996.
- HÉNON, M. 1966 Sur la topologie des lignes de courant dans un cas particulier. *C. R. Acad. Sci. Paris* **262**, 312–314.
- HEYMAN, J., LESTER, D.R. & LE BORGNE, T. 2021 Scalar signatures of chaotic mixing in porous media. *Phys. Rev. Lett.* **126**, 034505.
- HEYMAN, J., LESTER, D.R., TURUBAN, R., MÉHEUST, Y. & LE BORGNE, T. 2020 Stretching and folding sustain microscale chemical gradients in porous media. *Proc. Natl Acad. Sci.* **117** (24), 13359–13365.
- HOLM, D.D. & KIMURA, Y. 1991 Zero-helicity Lagrangian kinematics of three dimensional advection. *Phys. Fluids A: Fluid Dyn.* **3** (5), 1033–1038.
- HUI, W.H. & HE, Y. 1997 Hyperbolicity and optimal coordinates for the three-dimensional supersonic Euler equations. *SIAM J. Appl. Maths* **57** (4), 893–928.

- HUI, W.H. & KUDRIAKOV, S. 2001 A unified coordinate system for solving the three-dimensional Euler equations. *J. Comput. Phys.* **172** (1), 235–260.
- JANKOVIĆ, I., FIORI, A. & DAGAN, G. 2003 Flow and transport in highly heterogeneous formations: 3. Numerical simulations and comparison with theoretical results. *Water Resour. Res.* **39** (9), 1270.
- JANKOVIĆ, I., STEWARD, D.R., BARNES, R.J. & DAGAN, G. 2009 Is transverse macrodispersivity in three-dimensional groundwater transport equal to zero? A counterexample. *Water Resour. Res.* **45** (8), W08415.
- KANG, P.K., DENTZ, M., LE BORGNE, T. & JUANES, R. 2011 Spatial Markov model of anomalous transport through random lattice networks. *Phys. Rev. Lett.* **107**, 180602.
- LAMB, H. 1932 *Hydrodynamics*. Cambridge University Press.
- LE BORGNE, T., DENTZ, M. & CARRERA, J. 2008a Lagrangian statistical model for transport in highly heterogeneous velocity fields. *Phys. Rev. Lett.* **101**, 090601.
- LE BORGNE, T., DENTZ, M. & CARRERA, J. 2008b Spatial Markov processes for modeling Lagrangian particle dynamics in heterogeneous porous media. *Phys. Rev. E* **78**, 026308.
- LE BORGNE, T., DENTZ, M. & VILLERMAUX, E. 2013 Stretching, coalescence, and mixing in porous media. *Phys. Rev. Lett.* **110**, 204501.
- LE BORGNE, T., DENTZ, M. & VILLERMAUX, E. 2015 The lamellar description of mixing in porous media. *J. Fluid Mech.* **770**, 458–498.
- LESTER, D.R., BANDOPADHYAY, A., DENTZ, M. & LE BORGNE, T. 2019 Hydrodynamic dispersion and Lamb surfaces in Darcy flow. *Transp. Porous Med.* **130** (3), 903–922.
- LESTER, D.R., DENTZ, M., BANDOPADHYAY, A. & LE BORGNE, T. 2021 The kinematics of three-dimensional Darcy flow. *J. Fluid Mech.* **918**, A27.
- LESTER, D.R., DENTZ, M., BORGNE, T.L. & BARROS, F.P.J.D. 2018 Fluid deformation in random steady three-dimensional flow. *J. Fluid Mech.* **855**, 770–803.
- LESTER, D.R., DENTZ, M. & LE BORGNE, T. 2016b Chaotic mixing in three-dimensional porous media. *J. Fluid Mech.* **803**, 144–174.
- LESTER, D.R., TREFRY, M.G. & METCALFE, G. 2016a Chaotic advection at the pore scale: mechanisms, upscaling and implications for macroscopic transport. *Adv. Water Resour.* **97**, 175–192.
- LOWE, C.P. & FRENKEL, D. 1996 Do hydrodynamic dispersion coefficients exist? *Phys. Rev. Lett.* **77**, 4552–4555.
- MARSDEN, J.E. & HUGHES, T.J.R. 1994 *Mathematical Foundations of Elasticity*. Dover.
- MOFFATT, H.K. 1969 The degree of knottedness of tangled vortex lines. *J. Fluid Mech.* **1**, 117–129.
- NGUYEN-SCHFER, H. & SCHMIDT, J.-P. 2014 *Tensor Analysis and Elementary Differential Geometry for Physicists and Engineers*. Springer Publishing Company, Incorporated.
- OTTINO, J.M. 1989 *The Kinematics of Mixing: Stretching, Chaos, and Transport*. Cambridge University Press.
- PEYMIAT, C. & FONTAINE, D. 1999 A numerical method to compute Euler potentials for non dipolar magnetic fields. *Ann. Geophys.* **17** (3), 328–337.
- RANKIN, R., KABIN, K. & MARCHAND, R. 2006 Alfvénic field line resonances in arbitrary magnetic field topology. *Adv. Space Res.* **38** (8), 1720–1729.
- SOUZY, M., LHUISSIER, H., MÉHEUST, Y., LE BORGNE, T. & METZGER, B. 2020 Velocity distributions, dispersion and stretching in three-dimensional porous media. *J. Fluid Mech.* **891**, A16.
- SPOSITO, G. 1994 Steady groundwater flow as a dynamical system. *Water Resour. Res.* **30** (8), 2395–2401.
- SPOSITO, G. 1997 On steady flows with Lamb surfaces. *Intl J. Engng Sci.* **35** (3), 197–209.
- SPOSITO, G. 2001 Topological groundwater hydrodynamics. *Adv. Water Resour.* **24** (7), 793–801.
- TERNG, C.-L. & UHLENBECK, K. 1998 Introduction. In *Integrable Systems* (ed. C.-L. Terng & K. Uhlenbeck), Surveys in Differential Geometry, vol. 4, chap. 1, pp. 5–19. International Press.
- TURUBAN, R., LESTER, D.R., HEYMAN, J., LE BORGNE, T. & MÉHEUST, Y. 2019 Chaotic mixing in crystalline granular media. *J. Fluid Mech.* **871**, 562–594.
- TURUBAN, R., LESTER, D.R., LE BORGNE, T. & MÉHEUST, Y. 2018 Space-group symmetries generate chaotic fluid advection in crystalline granular media. *Phys. Rev. Lett.* **120** (2), 024501.
- VILLERMAUX, E. 2012 Out of equilibrium dynamics. Mixing by porous media. *C. R. Méc* **340** (11–12), 933–943.
- VILLERMAUX, E. & DUPLAT, J. 2003 Mixing is an aggregation process. *C. R. Méc* **331** (7), 515–523.
- WEATHERBURN, C.E. 1926 On Lamé families of surfaces. *Ann. Maths* **28** (1/4), 301–308.
- WINTER, H.H. 1982 Modelling of strain histories for memory integral fluids in steady axisymmetric flows. *J. Non-Newtonian Fluid Mech.* **10** (1), 157–167.
- YE, Y., CHIOGNA, G., CIRPKA, O.A., GRATHWOHL, P. & ROLLE, M. 2015 Enhancement of plume dilution in two-dimensional and three-dimensional porous media by flow focusing in high-permeability inclusions. *Water Resour. Res.* **51** (7), 5582–5602.

- ZAKHAROV, V.E. 1998 Description of the n -orthogonal curvilinear coordinate systems and Hamiltonian integrable systems of hydrodynamic type, I: integration of the Lamé equations. *Duke Math. J.* **94** (1), 103–139.
- ZIJL, W. 1986 Numerical simulations based on stream functions and velocities in three-dimensional groundwater flow. *J. Hydrol. (Amst)* **85** (3), 349–365.